INVESTIGATING THE GLOBAL GEOSPACE RESPONSE TO A PERIOD OF SOLAR WIND HIGH SPEED STREAMS USING THE LYON-FEDDER-MOBARRY MHD SIMULATION

by

KEVIN HUNG PHAM

Presented to the Faculty of the Graduate School of

The University of Texas at Arlington in Partial Fulfillment

of the Requirements

for the Degree of

DOCTOR OF PHILOSOPHY

THE UNIVERSITY OF TEXAS AT ARLINGTON

December 2014

Acknowledgements

I would like to first thank my supervising professor, Dr. Ramon E. Lopez, who has pushed me and believed in me throughout my doctoral studies. It has been incredibly motivating and encouraging to be a part of a big space physics research group and to also be a part of the greater space physics community.

I also would like to express my gratitude to my graduate committee: Drs. Yue Deng, Chris Jackson, Zdzislaw Musielak, and Alex Weiss. I am proud to share my research worth with an intellectual committee, and receive comments that help push my research into interesting directions.

Numerous friends have accompanied me along the way and I greatly appreciate their contribution to helping me understand physics and providing invaluable feedback on my research, including Robert Bruntz, Shree Bhattarai, Brian Bui, and Miguel Gomez. (Although some of my research ideas and understanding of physics may have been completely off-track.)

The funding during my Ph.D. research has been supported by CISM, which is funded by the STC program of the National Science Foundation under agreement ATM-0120950, NASA grant NNX09AI63G, NSF grant ATM-0900920 and GAANN grant P200A090284.

Finally, I would like to thank my family – my parents, my little brother, and my aunts and uncles – as well as my fiancée, Vy Huynh, for their constant support and encouragement. Thank you for providing a place to unwind and allowing me to study without worrying about finances and keeping my spirits high throughout.

November 24, 2014

Abstract

INVESTIGATING THE GLOBAL GEOSPACE RESPONSE TO A PERIOD OF SOLAR WIND HIGH SPEED STREAMS USING THE LYON-FEDDER-MOBARRY MHD SIMULATION

Kevin Hung Pham, PhD

The University of Texas at Arlington, 2014

Supervising Professor: Ramon E. Lopez

As the solar wind flows past the Earth, it interacts with the Earth's magnetic field and transfers energy and momentum to the geospace environment. During times when the solar cycle is near a minimum, there is a tendency for the Sun to produce high speed streams (HSSs), which are solar wind flows that are faster than the ambient solar wind. The HSSs contain properties that are not typically found in slower ambient solar wind, such as large amplitude Alfvén waves, that affect the transfer of energy and momentum. Large transfers of energy and momentum into the geospace environment that could lead to geomagnetic storms that affect technology that are used every day and possibly damage important global systems such as GPS. We used the Lyon-Fedder-Mobarry (LFM) 3D magnetohydrodynamic (MHD) simulation to study the response of the geospace and ionospheric environment in the presence of HSSs by performing a series of numerical experiments, consisting of simulations of the Whole Heliosphere Interval (WHI), which lasted from March 20 to April 16, 2008. We found that when the amplitude of the solar wind fluctuations were artificially enhanced, that although the total transferred energy increased, the efficiency of the energy transfer was reduced. We show that the

reduction in energy transfer efficiency is due to the increased presence of northward magnetic field when the fluctuation amplitudes are large. This conclusion is further supported by the results of a series of numerical idealized experiments that were conducted. The transfer of energy and momentum is regulated by the ionospheric Pedersen conductance. We show results from the LFM simulation that the generally accepted Pedersen conductance values are too low and cause the potentials produced by LFM to be too high.

.

Table of Contents

List of Illustrations

List of Tables

Chapter 1

Introduction

1.1 The Sun and Solar Wind

1.1.1 The Sun

The Sun is a dynamical object that effects everything within the solar system. At the solar core, Hydrogen nuclei are constantly undergoing nuclear fusion to produce Helium nuclei and generate energy. The energy eventually reaches the "surface" of the Sun (the photosphere), which has a temperature of about 6000K. Other processes, related to the transfer of mechanical energy of photospheric convection via the magnetic field produces a temperature in the Sun's corona of between one to three million K [Kivelson and Russell, 1995].

With a mass of about 330,000 times that of Earth's and a radius of about 696000 km or about 218 times Earth's radii (R_E), the Sun is only an average sized star. Although the Sun is large compared to the Earth, the radius of the Sun pales in comparison to the distance from the Sun to the Earth, which is approximately 149.6 million kilometers. Similar to the rotation of the Earth, the Sun also exhibits its own rotation. From the Earth's reference frame, the Sun makes one complete rotation about its axis on an average of 27 days but the solar pole and equator have different rotational periods, 35 and 25 days respectively [Philips, 1995].

The Sun has a magnetic field that is constantly changing. The presence of the solar magnetic field produces several phenomena such as sunspots, solar flares, and solar wind. Sunspots are spots on the Sun that appear visibly as dark regions. They appear darker than the surrounding regions due intense magnetic activity undergoing a convection effect and forming areas of reduced surface temperature. The magnetic activity causes strong heating of the solar corona, and the convection of the plasma may

cause twisting of magnetic field lines and generate magnetic stress that leads to intense solar flares and coronal mass ejections. Sudden releases from the solar surface of charged particles and electromagnetic radiation, ranging from X-rays and gamma rays through to visible light, are known as solar flares while coronal mass ejections (CME) are large clouds of strongly magnetized gas ejected out from the Sun's corona [Kivelson and Russell, 1995].

1.1.2 Solar Wind

The solar wind is constantly being ejected radially outwards from the Sun as a stream of ionized, highly conductive, and collisionless plasma. Solar wind flows are bimodal consisting of a slow and a fast solar wind [e.g., Lopez and Freeman, 1986]. Since the solar wind evolves as it propagate throughout the solar system, when the solar wind reaches Earth, the average slow solar winds have typical speeds of 400km/sec while average fast solar winds have typical speeds of 750km/sec [e.g., Gosling et al., 1995; Phillips et al., 1995]. The fast solar wind will also usually have lower densities than the slow solar wind, which has typical densities of 6.6 particle/cm^{-3} at 1 AU.

As the solar wind travels outwards from the Sun, it carries with it the Sun's magnetic field, known as the interplanetary magnetic field (IMF). The interaction between the solar wind's magnetic field and the Earth's magnetic field is important on the global scale and has effects ranging from forming the auroras at high latitudes to damaging satellites. In particular, the direction of the IMF has a strong effect on the rate of energy transferred from the solar wind to the magnetosphere.

One of the commonly used coordinate system used in space physics to study the interaction for the Sun-Earth system is the Geocentric Solar Magnetic (GSM) system. As illustrated in Figure 1.1, the center of the Earth is the origin of the coordinate system. The x-axis points from the origin to the center of the Sun; the z-axis is in the plane

defined by Earth's magnetic dipole axis and the x-axis; and the y-axis finishes the right-handed coordinate system. We refer to the z-component of the magnetic field as B_z and the y-component of the magnetic field as B_y. The B_z can further be broken into either northward or southward B_z that corresponds to either positive B_z or negative B_z, respectively.

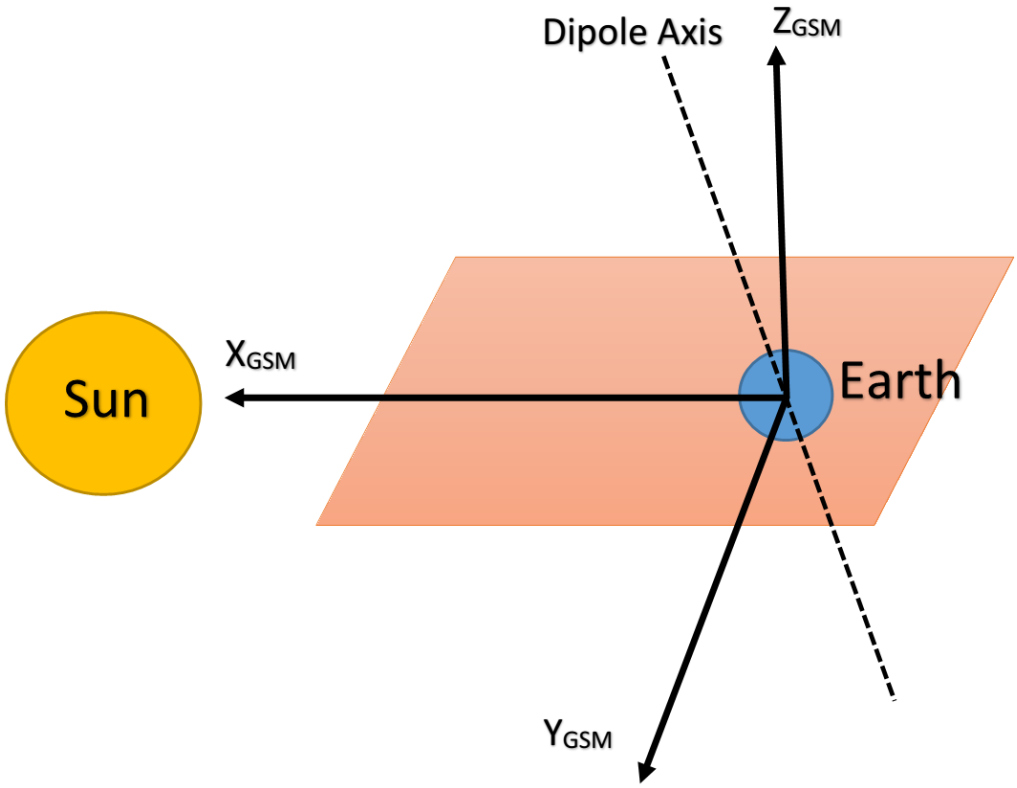

Figure 1.1 Schematic diagram of the GSM coordinate system.

1.1.3 MHD Waves

As the solar wind propagates through interplanetary space, it accelerates and becomes supersonic and superalfvénic before it reaches the Earth. Since the solar wind is a quasi-neutral fluid with very high conductivity, it behaves following magnetohydrodynamic (MHD) theory. The MHD wave modes are the sound waves,

Alfvén waves, and magnetosonic waves. Their associated speeds can be calculated (in MKS units) by using:

$$C_S = \sqrt{\frac{\gamma P_{sw}}{\rho_{sw}}} \qquad \text{(Sound Speed)} \qquad (1.1)$$

$$v_A = \frac{B_{sw}}{\sqrt{\mu_0 \rho_{sw}}} \qquad \text{(Alfvén Speed)} \qquad (1.2)$$

$$v_{MS} = \sqrt{v_A^2 + C_S^2} \qquad \text{(Fast Magnetosonic Speed)} \qquad (1.3)$$

where γ is the ratio of specific heats, P_{sw} is the solar wind plasma pressure, ρ_{sw} is the solar wind density, B_{sw} is the magnitude of the IMF, and μ_0 is the permeability of free space. The sound speed has a typical value of around 40 km/s and the Alfvén speed has a value of 48.8km/s for a solar wind with a density of 5 cm^{-3} and a magnetic field of 5 nT. This gives a typical sonic and Alfvén mach number of about 8 for the average solar wind speed of 400km/s.

These waves, in particular the Alfvén waves, are an important feature of the solar wind and may cause additional effects on the magnetosphere-ionosphere system besides the solar wind velocity and IMF. Close to the Sun, Alfvén waves contain enough energy to be the main driving force behind acceleration of fast solar winds and heating of the corona [McIntosh et al., 2011]. Once the solar wind flow is supersonic and superAlfvénic, the waves are carried outward by the flow. As the embedded Alfvén wave propagate in the solar wind, it perturbs the plasma velocity and IMF, which we refer to as the Alfvénic fluctuations [e.g., Blecher and Davis, 1971]. The perturbations in the plasma velocity and IMF are correlated and the sign of their correlation depends on whether the IMF vector is pointing towards or away from Earth.

1.1.4 Solar Cycle

The solar magnetic field varies every year and reverses its polarity every eleven years during solar maxima. Solar maximum and solar minimum corresponds to the number of sunspots. During solar maxima, the occurrence rate of CMEs is higher than solar minima [Webb and Howard, 1994] and CMEs are the dominant source of geomagnetic activity. While during solar minima, the dominant source of geomagnetic activity comes from corotating interaction regions (CIR) and high speed streams (HSS). The solar wind is considered to be an HSS when the solar wind velocity is above 500 km/s.

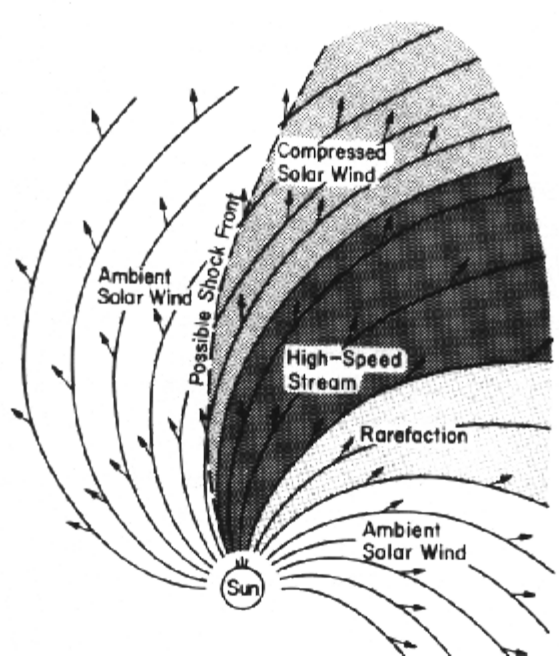

Figure 1.2 Schematic of an HSS interacting with slower solar wind infront, creating a compressed region [Hundhausen, 1972].

HSSs originate from coronal holes, regions of unusually low density and high temperature in the solar corona, but it is unknown whether they originate at the edge or center of coronal holes [Zirker, 1977]. HSSs also contain large amplitude Alfvén waves

that cause large perturbations affecting the influence of the solar wind on the magnetosphere-ionosphere system [Belcher and Davis, 1971; Richardson, 2006]. Since coronal holes can last for several months, they produce recurring activity corresponding roughly to a Carrington rotation (the average solar rotation), or 27 Earth days.

As seen in Figure 1.2, the HSS propagates outwards and catches up to slower solar wind ahead. The HSS piles up the slower solar wind in front and creates a compressed interface known as a Corotating Interaction Region, or CIR. Both the HSS and the ambient solar wind are propagating radially outwards and since the HSS originates from coronal holes on the Sun, then when the Sun rotates, so does the HSS's origin. Due to this, when we progress to the next moment in time, the coronal has moved one spatial location while the HSS that was previously ejected has moved radially outwards one spatial step. This creates the spiral appearance seen in Figure 1.2 and because the coronal holes rotate with the Sun, the compressed interface corotates with the Sun. The compression in the CIR can steepen into a shock, and the compressed magnetic fields can drive geomagnetic activity. Following the CIR, the HSS usually has high level of Alfvénic turbulence, which can produce geomagnetic storms [e.g. Tsurutani 2006; Richardson, 2006].

1.2 The Magnetosphere

In the reference frame of the Earth, the solar wind is traveling at supersonic speeds. When the supersonic solar wind encounters the Earth's magnetic field, it decreases to subsonic speeds and forms a bow shock. The bow shock is located on the dayside of the Earth and in front of the Earth's magnetic field. In order for the solar wind plasma to become subsonic, while conserving total energy, momentum and mass, the

solar wind plasma must become heated, compressed and the magnetic field strength must also increase as it transitions pass the bow shock.

Immediately after passing the bow shock, the solar wind flows through a region of subsonic solar wind plasma called the magnetosheath. These regions can be seen in Figure 1.3. The magnetosheath shape and size depends strongly on both the properties of the upstream solar wind conditions and the ionospheric conductivity. The plasma contained in the magnetosheath is still the solar wind plasma and solar wind magnetic field.

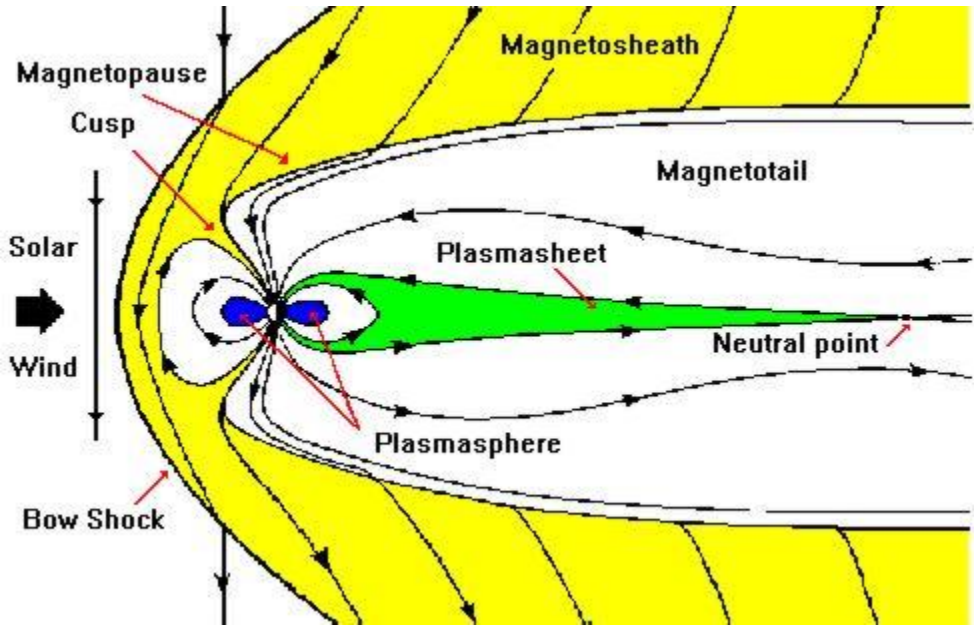

Figure 1.3. A diagram of the X-Z plane of the magnetosphere.

The boundary that separates solar wind magnetic field and the Earth's magnetic field is called the magnetopause. This region is where it transitions from solar wind plasma and magnetic field to Earth's plasma and magnetic field. The location of the

magnetopause depends on where the forces on both sides of the boundary are balanced, therefore will vary with solar wind conditions.

Most of the solar wind plasma is deflected at the boundary and only a small portion of the solar wind plasma and energy penetrates and transfers into the magnetosphere. Since the magnetopause separates regions of different magnetic field magnitude, and perhaps orientation, by Amperes' law, there must be a current that flows along the boundary. This current is known as the Chapman-Ferraro current [e.g., Kivelson and Russell, 1995]. The currents are dependent on the solar wind dynamic pressure and the amount of coupling between the IMF and the geomagnetic field.

The equation estimating the point of the magnetopause that is on the Sun-Earth line is given by pressure balance between the solar wind flow pressure and the geomagnetic field pressure from Earth's dipole. This yields the distance along the Earth-Sun line (known as the standoff distance) to be:

$$r \approx \sqrt[6]{\frac{2B_0^2}{\mu_0 \rho v^2}} \tag{1.4}$$

where r is the standoff distance, μ_0 is the permeability of free space, B_0 is the strength of Earth's magnetic field, ρ is the solar wind density, and v is the solar wind velocity. When the solar wind dynamic pressure is lower, the magnetopause moves further away. With a weaker geomagnetic field at the further location, the Chapman-Ferraro currents are also weakened. The flanks of the magnetopause is shaped by the strength of the Chapman-Ferraro currents and the ionospheric conductivity. The size of the tail is determined by pressure balance between the magnetic field in the tail lobes and the thermal plasma pressure in the magnetosheath.

The magnetosphere is the region that is dominated by the Earth's magnetic field. Similar to the other magnetospheric structures, such as the bow shock, magnetosheath

and magnetopause, the magnetosphere's shape is controlled by the solar wind upstream plasma conditions, the Earth's magnetic field strength, and the ionospheric conductivity. The general shape of the magnetosphere is similar to that of a comet. The dayside, the side of the Earth that is facing the Sun, of the magnetosphere is hemispherical in shape that changes into a long cylinder shape on the night side that aligns with the solar wind flow.

1.3 The Ionosphere and Current System

The ionosphere is a region in the upper atmosphere that is ionized mostly by solar radiation. The solar radiation ionizes gas molecules and populates this region with a high concentration of electrons causing the ionosphere to be electrically conducting. The ionosphere's altitude ranges from about 60km to 1000km and can be subdivided into D, E, and F layers. Each layer corresponds to different physical processes and atmospheric density. The F layer is the only layer that has significant amount of ionization at night while all three layers are much more ionized during the day than the nighttime F layer.

One of the major locations where the Chapman-Ferraro currents close is the ionosphere. The Chapman-Ferraro currents enter and leave the ionosphere via Birkeland currents, which are currents aligned along the geomagnetic field (named after Kristian Birkeland), and close through Pedersen currents (currents parallel to **E**). Figure 1.4 shows both the Birkeland, the Pedersen, and the Hall currents (current perpendicular to **E**). In the ionosphere, the associated conductivities are the Pedersen conductivity and the Hall conductivity.

As seen in Figure 1.4, the Birkeland currents can be further broken down into various regions. The main two regions that are present at all times are the region 1 and

region 2 currents. Region 1 currents are at high latitudes and flow downward on the dawn side while upward on the dusk side. Region 2 currents are at lower latitudes and, more importantly, have the opposite polarity as region 1; downward on the dusk side and upward on the dawn side. While the Region 1 currents are associated with the outer magnetospheric current systems, like the Chapman-Ferraro current system, the Region 2 currents are associated with the inner magnetosphere current system and, in particular, the currents driven by plasma pressure gradients.

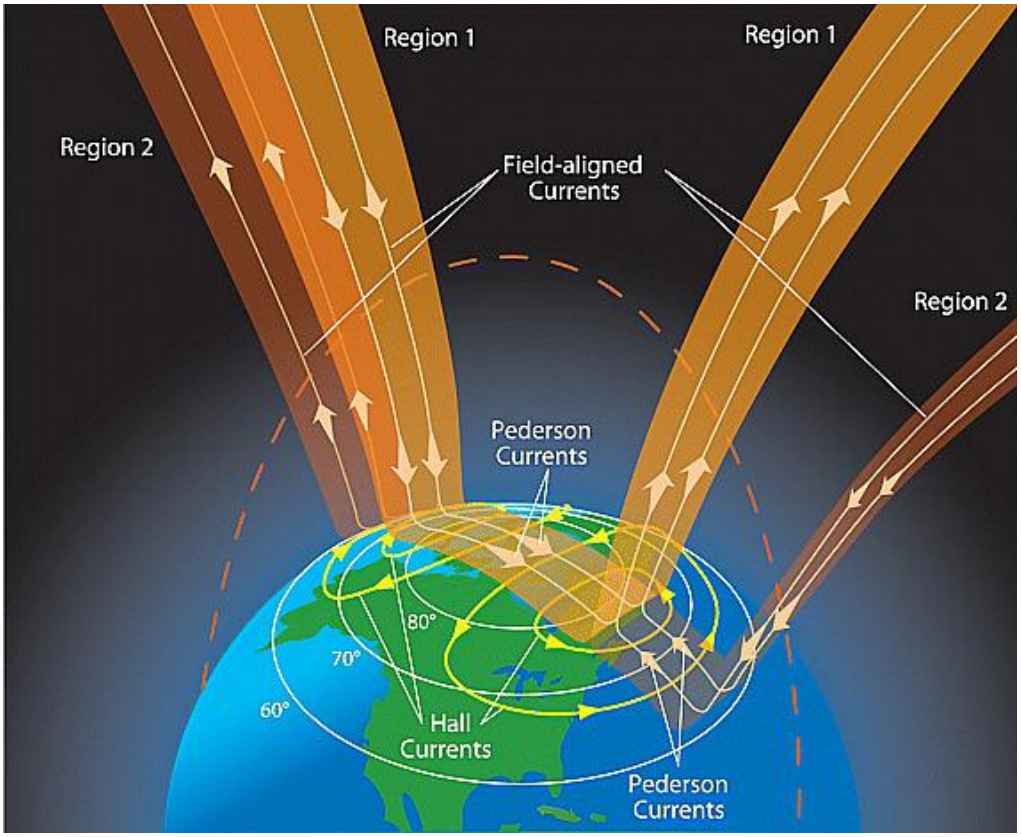

Figure 1.4. Diagram of the different ionospheric current systems [Figure 1 from Le et al., 2010].

Differences in the local density of the plasma on the nightside of the Earth give rise to pressure gradients that cause the particles in the inner magnetospheric plasma to drift. The pressure gradients form a current that can be determined from the MHD momentum equation (see equation (2.2)), which is given by:

$$\overrightarrow{v_D} = -\frac{\nabla p \times \vec{B}}{qnB^2} \tag{1.5}$$

where ∇p is the pressure gradient of the particles and B is the local magnetic field. The divergence of this current is what gives rise to the Region 2 current.

There also exists a region 0 current system that is at the very high latitudes (above region 1) and it has region 2 polarity [Iijima and Potemra, 1976]. These region 0 current occur during periods of northward B_z and are associated with the reverse convection cell that are caused by magnetic reconnection with the northward IMF [e.g., Bhattarai et al., 2012].

1.4 Space Weather

As society becomes increasingly more space-based, our understanding and ability to accurately predict the space weather and space environment also becomes increasingly more important. Just like weather on Earth, space weather is extremely dynamic and is constantly occurring all around us. Although we are unable to directly see space weather, like we can with terrestrial weather, space weather has consequences that may drastically affect life on Earth.

One area that that space weather will severely impact is industry. For example, the airline industry will divert flights away from polar regions during disturbed space weather conditions. When the space weather conditions are severe, it could cause high frequency radio black-outs in the polar regions which would be dangerous for pilots and

there would be increased radiation in the polar region that would affect everyone on board the flights [Carlowicz and Lopez, 2002]. Although most passengers will not exceed their lifetime allowance for radiation, pilots and crewmembers may eventually surpass their allocation after many flights.

Perhaps the most important possible effect of space weather would be damage to electrical power grids on Earth. Severe space weather conditions could potentially cause large-scale power blackouts and destroy transformers that would lead to permanent damage [Space Studies Board, 2008]. By effectively predicting space weather, we can prevent power grid failure by balancing the load on the power grid ahead of the event.

As the Sun is approaching a solar minimum, high speed streams will dominate the space weather environment. High speed streams are particularly dangerous to spacecraft as they bring highly energetic electrons that can cause a phenomenon known as spacecraft charging. Spacecraft charging will cause various surfaces in the spacecraft or satellite to become electrically charged and damage electronics that are onboard [Space Studies Board, 2008]. For example, if the GPS satellites were to be damaged, then the effects would be widespread throughout our society [Carlowicz and Lopez, 2002].

We are interested in improving our understanding of space weather caused by these high speed streams and other phenomena. A better understanding of the dynamics and energy transfer during these periods would allow us to better understand the situation. This would lead to greatly improved computer simulations and models that will help advance our capability to predict when the events will occur and how devastating an event may be.

1.5 Solar Wind and Magnetosphere Interactions

There are two major interactions that drive the solar wind-magnetosphere system, the viscous interaction and the magnetic reconnection. Both interactions act on the system through electromagnetic and mechanical forces to cause the plasma and the magnetic field lines in the magnetosphere to circulate, thus transferring energy and momentum from the solar wind flow to the magnetosphere.

Circulation and convection of the plasma will impose an electric field in Earth's high-latitude ionosphere. In Earth's reference frame, the Birkeland currents put stress on the surrounding plasma and sets the plasma into motion. For a frozen in flux situation, the motion of the plasma means that there must be an electric field In Earth's frame of reference such that the resulting plasma velocity is $v = \frac{E \times B}{B^2}$. Integrating the electric field over a given distance will determine the electric potential in the ionosphere between any two points. This electric potential, known as the transpolar potential (TPP), and the integrated Birkeland currents (IBC) are good measures of the amount of energy and momentum transferred into the magnetosphere by the solar wind. The IBC is an integration of the Birkeland current over the entire ionosphere. Both the IBC and TPP behave similarly and any description of TPP can also be applied to the IBC.

1.5.1 Viscous Interaction

As the solar wind flows pass the Earth, it drags the magnetosheath plasma on the flanks along and accelerates the plasma to supersonic speed while traveling tailward. The velocity shear between the plasmas on either side of the magnetopause produces Kelvin Helmholtz waves. These Kelvin-Helmholtz waves cause the plasma on the magnetosphere side of the magnetopause to start moving anti sunward and circulate [e.g. Claudepierre et al., 2008]. This viscous convective flow produces a magnetic shear that generates a current system that maps into the ionosphere with Region 1 polarity

(current flows into the ionosphere at dawn and flows out at dusk). The stress transmitted to the ionosphere from this current contributes to the net forces on the flow of the plasma and so it contributes to the TPP. We refer to the contribution to the TPP by the viscous interaction as the viscous potential (VP). The viscous interaction is purely mechanical so the orientation of the convection cells are independent of the IMF orientation. For both orientations of the y-component of the IMF as well as the southward IMF, VP is independent of the IMF strength [Mitchell et al., 2010; Bruntz et al., 2012a].

For purely northward IMF, there is no magnetic reconnection occurring at the nose of the magnetosphere to reduce the plasma density. The increased density at the nose is greater than the nearby local time sectors, creating a pressure gradient that points away from noon. This causes plasma to be accelerated antisunward and reduces the velocity shear across the magnetopause, resulting in a reduction in the viscous potential for northward IMF [Bhattarai and Lopez, 2013].

1.5.2 Magnetic Reconnection

Magnetic reconnection occurs when the magnetic topology of highly conducting plasma is rearranged and converts magnetic energy into kinetic energy, thermal energy, and particle acceleration. Dungey [1961] first proposed that magnetic reconnection was the driver for solar wind-magnetosphere interaction. Motion of plasma will move the magnetic field lines that are trapped in the plasma and the inverse is also true, that motion of magnetic field lines will move the plasma that is trapped on the field line, this is called the frozen-in flux condition. When two oppositely oriented magnetic field lines are pushed together, the magnetic field lines from each field will become broken and then reconnect with the other field. Due to the frozen-in flux condition, this reconnection of two different magnetic field lines will allow plasma trapped on one magnetic field line to move to the other magnetic field line, energizing the plasma in the reconnection region.

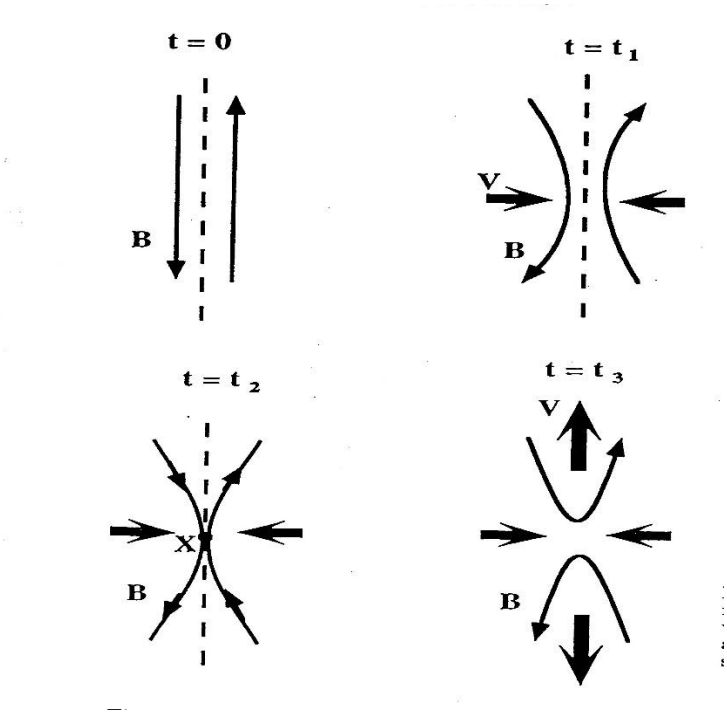

Figure 1.5 Diagram of the process of magnetic reconnection in two-dimensional space.

1.5.3 IMF Orientation

Although the types of interactions are the same, southward B_z and northward B_z will each configure the magnetosphere differently. For southward B_z, magnetic reconnection occurs at the magnetopause on the equatorial plane, and there is another site for magnetic reconnection down the magnetotail, on the Sun-Earth line. The line of reconnection that forms on the magnetopause is known as the reconnection line. If we project the reconnection line back into the solar wind, the resulting length of the projection that is parallel to the solar wind electric field, found from $E = -v \times B$, is the geoeffective length L_G [Burke et al., 1999; Lopez et al., 2010]. Figure 1.6 provides a good visual representation of this concept. The potential that is applied across the reconnection line, or reconnection potential, can then be found by taking LG times the solar wind electric field.

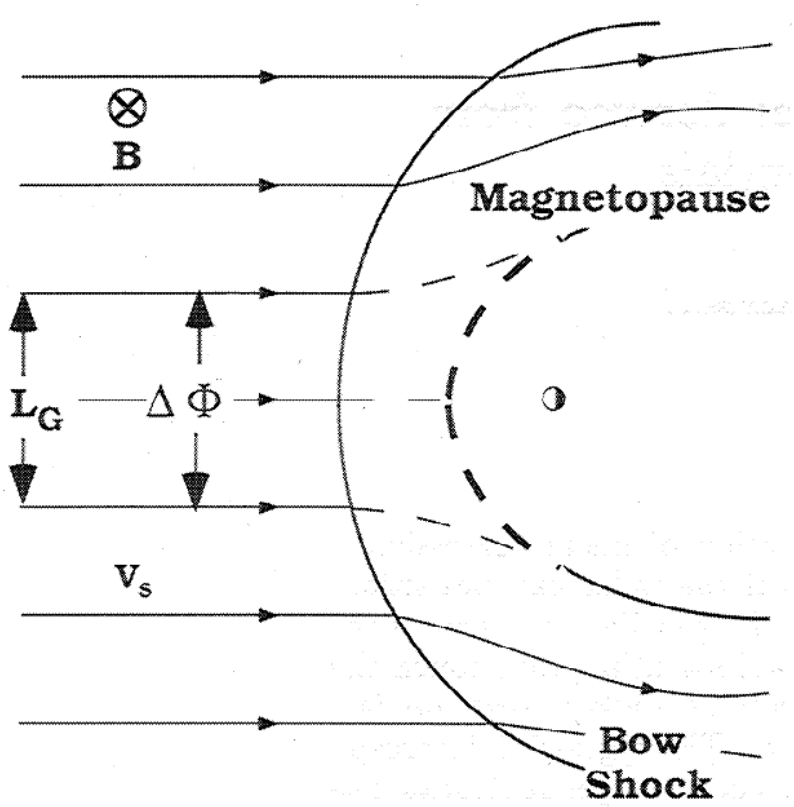

Figure 1.6 Projection of the reconnection line at the magnetopause back into the solar wind, known as the geoeffective length L_G. [From Figure 1 in Burke et al., 1999]

The viscous potential depends on the solar wind velocity and density but is independent of how strongly southward the magnetic field is. On the other hand, the reconnection potential depends on the strength of the southward magnetic field. The reconnection potential increases with larger B_z magnitudes but at large values of B_z, the reconnection potential exhibits saturation effect where increasing the magnitude of B_z will not cause the reconnection potential to increase. This saturation effect occurs for large values of northward and southward B_z, and also for B_y.

Except for saturation, northward B_z affects the potential differently than southward B_z. Unlike for southward B_z where the reconnection potential occurs at the magnetopause on the equatorial plane, reconnection for northward B_z occurs near the

polar cusps in both the northern and southern hemisphere. This causes the reconnection potential cells to be opposite polarity than that for southward B_z. When the reconnection and viscous cells have the same polarity, then the measured TPP is the sum of the viscous and the reconnection potentials but when the cells have opposite polarity then the measured TPP will be the greater of the two.

The viscous potential during periods of northward B_z does not stay constant like when the B_z is southward. In fact, northward B_z causes the viscous potential to decrease with increasing northward B_z [Bhattarai and Lopez, 2013]. As shown in Figure 1.7, at low values of northward B_z (this threshold changes with solar wind conditions), the viscous potential dominates over the reconnection potential; therefore the measured TPP is purely viscous. At these low values of northward B_z, the viscous potential is seen to continually decrease until it is overtaken by the reconnection potential. Once the reconnection potential has overtaken the viscous, it continues to rise until reaching saturation. By looking at the ionospheric convection cells, Bhattarai et al. [2012] was ascertain that the viscous potential continued to decrease at all values of northward B_z.

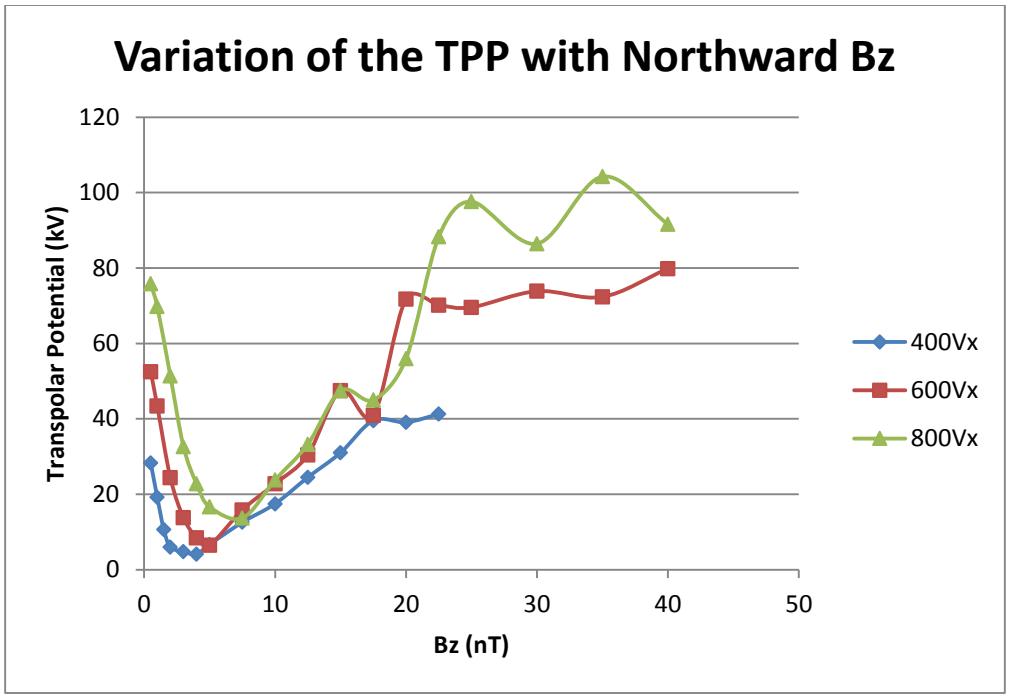

Figure 1.7 Saturation of the TPP with increasing B_z for different solar wind velocities obtained from simulation [Figure 3 from Bhattarai and Lopez, 2013].

Chapter 2

Lyon-Fedder-Mobarry Simulation

The amount of space between Earth and the Sun is enormous compared to the instruments we use to measure the effects from the interaction between the solar wind and the geomagnetic field. It is practically impossible to create an array of satellites that can effectively provide a 3-D picture of what is happening in the magnetosphere. Since it is not possible to control the Sun and what the solar conditions are, computer simulations have been created and are continually being developed to study the global effects of solar wind and magnetosphere interactions. In this study, we used the Lyon-Fedder-Mobarry (LFM) 3-D magnetohydrodynamic (MHD) simulation of the Earth's magnetosphere. LFM has been in development since the mid-1980s and improvements are continually to being made [Lyon et al., 2004].

2.1 MHD Equations

The simulation treats the ideal collionless plasma as a fluid that is described by MHD equations. These MHD equations are, essentially, standard hydrodynamic equations that are modified using Maxwell's equations and Ohm's Law. The equations typically take the form of:

$$\frac{\partial \rho}{\partial t} + \nabla \cdot \rho \boldsymbol{u} = 0 \qquad \text{(Mass Conservation)} \qquad (2.1)$$

$$\rho\left(\frac{\partial \boldsymbol{u}}{\partial t} + \boldsymbol{u} \cdot \nabla \boldsymbol{u}\right) = -\nabla \cdot \boldsymbol{p} + \boldsymbol{J} \times \boldsymbol{B} \qquad \text{(Momentum Equation)} \qquad (2.2)$$

$$\nabla \times \boldsymbol{B} = \mu_0 \boldsymbol{J} \qquad \text{(Ampere's Law)} \qquad (2.3)$$

$$\frac{\partial \boldsymbol{B}}{\partial t} = -\nabla \times \boldsymbol{E} \qquad \text{(Faradays' Law)} \qquad (2.4)$$

$$\boldsymbol{E} + \boldsymbol{u} \times \boldsymbol{B} = 0 \qquad \text{(Ideal Ohm's Law)} \qquad (2.5)$$

where ρ is the mass density, **u** is the center of mass velocity, **p** is the plasma pressure tensor, **J** is the current density, **B** is the magnetic field, and **E** is the electric field [Lyon et al., 2004]. Equation (2.1) simply states that there are no sources of sinks inside of the system such that the rate of flow into the system must equal the rate of flow out of the system except for what stays inside. The next equation, equation (2.2), relates the change in the momentum in the flow to the net force of the flow. In the case that the plasma is stationary, the equation reduces to the balance between plasma and the **JxB** force. Equation (2.3) describes that an electric current can be produced by taking the curl of the magnetic field while equation (2.4) is simply the Maxwell equations and shows that a magnetic field changing in time will generate an electric field. Equation (2.5) is also known as the frozen-in flux condition where flux through plasma is trapped in the plasma. This implies that when the plasma is in motion, that motion also describes the motion of the magnetic field. To numerically solve these equations, LFM uses a form of the equations that are slightly modified from the above but allow computers to properly process.

2.2 LFM Simulation Boundary and Grid

Although the grid resolution and dimensions of LFM can be changed, the grid is typically set with Earth at the origin and extends 25 R_E towards the Sun, 300 R_E away from the Sun, and 100 R_E on the sides. The LFM grid, shown in Figure 2.1, is a nonadaptive distorted spherical grid with the lowest resolution grid being 50 points radially, 32 points azimuthally, and 24 points latitudinally. This type of grid structure allows for the grid points to be concentrated in regions of interest and sparse in regions

that are less significant in model development while reducing the amount of computation time required to solve the entire system.

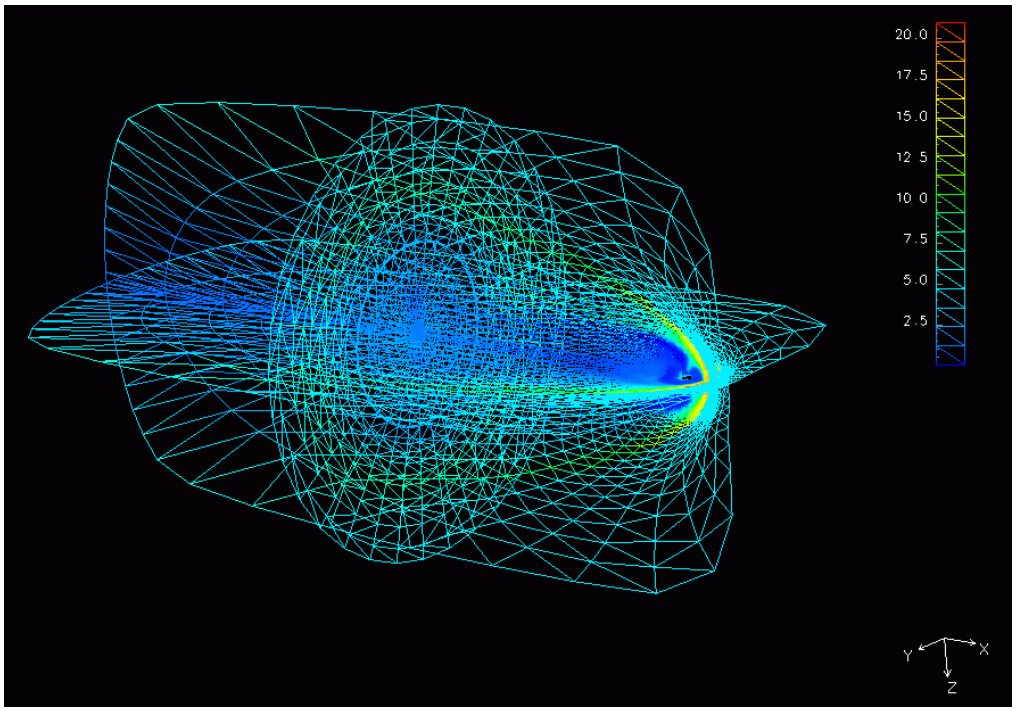

Figure 2.1 Three cutplane view of the LFM grid where grid points are connected by lines.

The cell size decreases and becomes denser near Earth, to help resolve important regions such as the magnetopause and structures within the magnetosheath, and stretches to large cell sizes down the magnetotail, as seen in Figure 2.2. The timestep is restricted by the speed of the fastest wave in the simulation such that in one timestep, the wave does not travel across multiple grid cells. Reducing the timestep will cause the computation time to also increase. Therefore, the amount of computational power and computation time that are available will restrict the timestep and the grid size. If the grid was doubled in resolution, then the penalty to computation time is approximately 16 times. Each direction will have increased by a factor of 2 and the timestep must also be decreased by a factor of 2, causing the computation time to

increase by at least 16 times. Although the computation time can be offset by increasing the number of computer cores, most codes and computer architecture do not scale linearly with increasing number of cores.

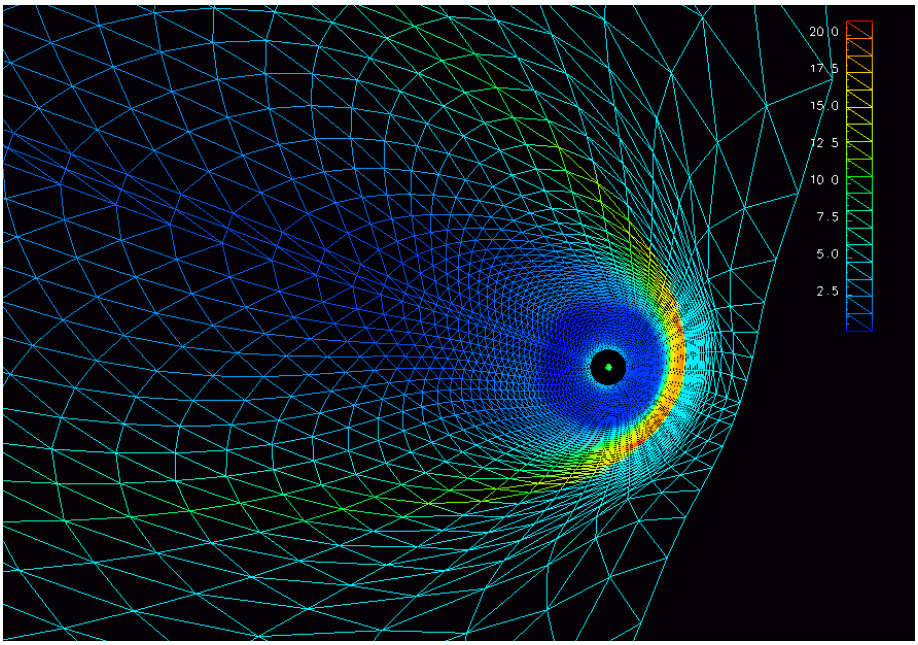

Figure 2.2 An equatorial cutplane view of the LFM grid with lines connecting grid points.

The LFM grid contains an outer and an inner boundary. The outer boundary is approximately a cylindrical surface that encloses the simulation domain while the inner boundary is a sphere of about 2.8 R_E around Earth. If the inner boundary is too close to the Earth, the timestep required to resolve any waves would cause amount of computation time to be unfeasible. The “front” of the LFM boundary, or the sunward surface of the outer boundary, is fed solar wind conditions from an external solar wind file that are then propagated along the LFM domain and out the “back” or tailward side of the boundary. Since the solar wind flow is supersonic and super-Alfvénic, no information in the solar wind can flow sunward; therefore the back of the LFM domain is for outflow

only, no inflow is allowed. The solar wind file contains either idealized solar wind conditions, real solar wind data from satellite measurements (such as ACE or WIND), or the output from solar wind simulations and models.

When using real solar wind data or data from models, there is no initialization done, but it is normal to include approximately 12 hours of data that precedes the event being simulated. By including the extra 12 hours of data, it allows the simulation to properly initialize and be within realistic starting conditions as the real event. For idealized solar wind conditions, the simulation is initialized with 2 hours of -5nT Bz to empty the magnetosphere of plasma through magnetic reconnection followed by 6 hours of +5nT Bz to load the magnetosphere with plasma.

2.3 Ionospheric Simulation

The inner boundary of LFM maps directly along magnetic field lines to a 2-D ionospheric simulation model. Below the inner boundary (of 2.8 R_E), the plasma is no longer considered to be infinitely conducting and therefore the conductivity takes finite values. Field aligned currents (Birkeland currents) and the just introduced ionospheric conductivity are used to solve for the ionospheric potential in the equation:

$$\nabla \cdot \underline{\Sigma} \cdot \nabla \phi = j_{||} sin\delta \tag{2.6}$$

where ϕ is the electrostatic potential, δ is the dip angle, and $\underline{\Sigma}$ is the conductivity tensor.

The conductivity tensor contains a component for the direction parallel to the surrounding magnetic field and another component for perpendicular to the magnetic field. The electric field induced by ionospheric currents transforms the tensor, resulting in:

$$\underline{\boldsymbol{\Sigma}} = \begin{pmatrix} \dfrac{\boldsymbol{\Sigma_P}}{\sin^2 \delta} & -\dfrac{\boldsymbol{\Sigma_H}}{sin\delta} \\ \dfrac{\boldsymbol{\Sigma_H}}{sin\delta} & \boldsymbol{\Sigma_P} \end{pmatrix} \tag{2.7}$$

where $\underline{\Sigma}_P$ is the Pedersen conductivity and $\underline{\Sigma}_H$ is the Hall conductivity. Pedersen conductivity and associated currents, are perpendicular to the magnetic field but parallel to the electric field while Hall conductivity and associated currents are perpendicular to both magnetic and electric fields. Hall currents typically form in closed loops within the ionosphere and do not contribute very much to equation (2.6). Birkeland currents enter the ionosphere, flow across the ionosphere as Pedersen currents, and then flow out of the ionosphere as Birkeland currents again.

Although LFM can be coupled to various ionospheric models, the LFM simulation itself contains two possible conductivity models. The first model is an idealized conductance model in which the Pedersen conductivity, set at the beginning, is a constant and uniform value over the entire ionosphere. The second is a semi-empirical model that uses the solar F10.7 flux as an input. The solar F10.7 flux is a measure of the solar radio emission at the 10.7 cm wavelength and given in units of solar flux units (SFU). For the semi-empirical model, particle precipitation is allowed to affect the conductivity. The resulting conductance is then the square root of the sum of the squares of the conductivities from particle precipitation and F10.7 flux [Fedder et al., 1995].

2.4 Conductance Problem

Measuring the conductance directly is extremely difficult if not currently technologically impossible. However, an estimate of the conductance (or conductivity) can be calculated from data collected from incoherent scatter radar, all-sky cameras at 557.7 nm, or satellites [e.g. Brekke et al., 1974; Brekke et al., 1988; Kosch et al., 1998; Aksnes et al., 2005]. These calculations are essentially simple models that are made by

making assumptions in order to obtain a conductance from the collected data. Some models will result in a conductance that depends on the solar zenith angle, or the angle the Sun makes from the normal to the Earth's surface. In the polar area, the zenith angle only travels from approximately 50 to 90 degrees. At these angles, the Pedersen conductance is approximately between 2 mhos and 8 mhos [e.g. Vickrey et al., 1981; Lilensten et al., 1996; Aksnes et al., 2005; Aikio and Selkala, 2009] or an average of about 5 mhos. This average of 5 mhos is outputted by most conductance models [e.g. Brekke and Moen, 1993; Reiff, 1984] and is considered to be the standard condition for the Pedersen conductance [e.g. Kamide and Richmond, 1982].

When the LFM simulation is run with constant Pedersen conductance of 5 mhos, the resulting the TPP is seen to be between 50% to 100% greater than realistic values [e.g. Lopez et al., 1990; Fedder et al., 1998; Bruntz et al., 2012a; Bruntz et al., 2012b; Lopez et al., 2012]. It was found that setting the constant Pedersen conductance to 10 mhos, the TPP values were in good agreement with reality [e.g., Lopez et al., 2010]. Many LFM simulation users solve this TPP issue by doing their studies using both 5 mhos and 10 mhos [e.g. Merkin et al., 2003; Lopez et al., 2010; Bruntz et al., 2012a; Bhattarai et al., 2012]. Rather than using a constant ionospheric conductance model, it was found that when using an empirical ionospheric model that the resulting TPP was still far higher than reality [Wiltberger et al., 2012]. Other MHD models also obtained potential values that were too high [Raeder et al., 1998] while another model acknowledges the problem and attempts to fix the problem by imposing an artificial region 2 current to force the potentials lower [Ridley et al., 2002]. This raises the possibility that the ionospheric conductance calculated by ionospheric models are too low.

2.5 Magnetopause Study

The ionospheric conductance regulates the Birkeland currents that flow into and out of the ionosphere. The Chapman-Ferraro current system flow from the magnetopause and closes along the Birkeland currents. This current system helps balance the magnetic and mechanical forces from the solar wind on the front of the magnetosphere. Since these currents close along Birkeland currents, changing the ionospheric conductance would affect the strength of the forces and therefore affect the position and shape of the magnetopause. To verify whether 5 mhos is too low of a conductance or if it is simply a problem with the TPP, we compare the simulation magnetopause with an empirical fit of the magnetopause. We simulated standard solar wind conditions (-400km/s V_x, 0km/s V_y, 0km/s V_z, 5 particles cm^{-3}) and a magnetic field strength of -1nT and -3nT B_z.. The ionospheric Pedersen conductance was varied using a range of values between 5 mhos and 10 mhos.

2.5.1 Empirical Magnetopause Fit

Using data from a variety of sources, Sibeck et al. [1991] determined a fit to 1821 magnetopause crossings. Each magnetopause crossing was matched to the respective solar wind dynamic pressure and magnetic field strength. The fits were then binned into different ranges of solar wind dynamic pressure and magnetic field strength. The solar wind dynamic pressure changed the position of the subsolar point of the magnetopause while the magnetic field strength changes how much flaring there is on the flank of the magnetopause. Since the only variable in our study is the Pedersen conductance, using either the binned solar wind dynamic pressure or the binned magnetic field strength is enough. We arbitrarily chose to use the magnetic field strength bin. Table 2.1 shows the different Bz ranges, the number of magnetopause crossings data used, and the coefficients obtained from the fit.

Table 2.1 Magnetopause fits of the form $R^2 + Ax^2 + Bx + C = 0$ and binned by IMF values. [From Table 3 in Sibeck et al., 1991]

IMF Range, nT	Points	A	B	C	σ	Subsolar Point	Dawn Meridian
$-6 < B_z < -4$	59	0.12	19.9	−200.6	1.9	9.6	14.2
$-4 < B_z < -2$	154	0.22	18.2	−213.4	1.9	10.4	14.6
$-2 < B_z < 0$	263	0.11	17.9	−212.8	1.9	11.1	14.6
$0 < B_z < 2$	271	0.20	17.1	−221.5	1.9	11.5	14.9
$2 < B_z < 4$	115	0.09	15.7	−198.3	2.0	11.8	14.1
$4 < B_z < 6$	53	0.13	13.1	−179.2	2.4	12.2	13.4

Since the subsolar point depends on the solar wind dynamic pressure, Sibeck et al. [1991] does not specify the solar wind dynamic pressure for each IMF range and so we assume that the solar wind dynamic pressure in our simulation is different than that provided in Table 2.1. To account for this, we manually adjust the subsolar point of the magnetopause fit to match with the subsolar point in the LFM simulation results. The magnetopause can be identified in the simulation by mapping contours for where B_z is 0nT. The B_z = 0 nT boundary is where there is a magnetic shear, meaning that plasma transitions from the solar wind's magnetic field to the geomagnetic field.

From the simulation results using -3Bz and -1Bz for various Pedersen conductance, we can see that the 10 mhos simulations match with the Sibeck et al. [1991] magnetopause fits better than the lower conductance. Although the 5 mhos conductance gives a seemingly better match, there is more overlap between the two lines for 10 mhos. Since these magnetopause fits are not derived using the TPP, they provide another line of evidence to support the argument that a 10 mhos Pedersen conductance is more realistic than the often used 5 mhos. We arrive at the conclusion that using a 5 mhos conductance is an underestimation of the ionospheric conductance and that ionospheric models must be missing a key contributor to the calculation of the Pedersen conductance.

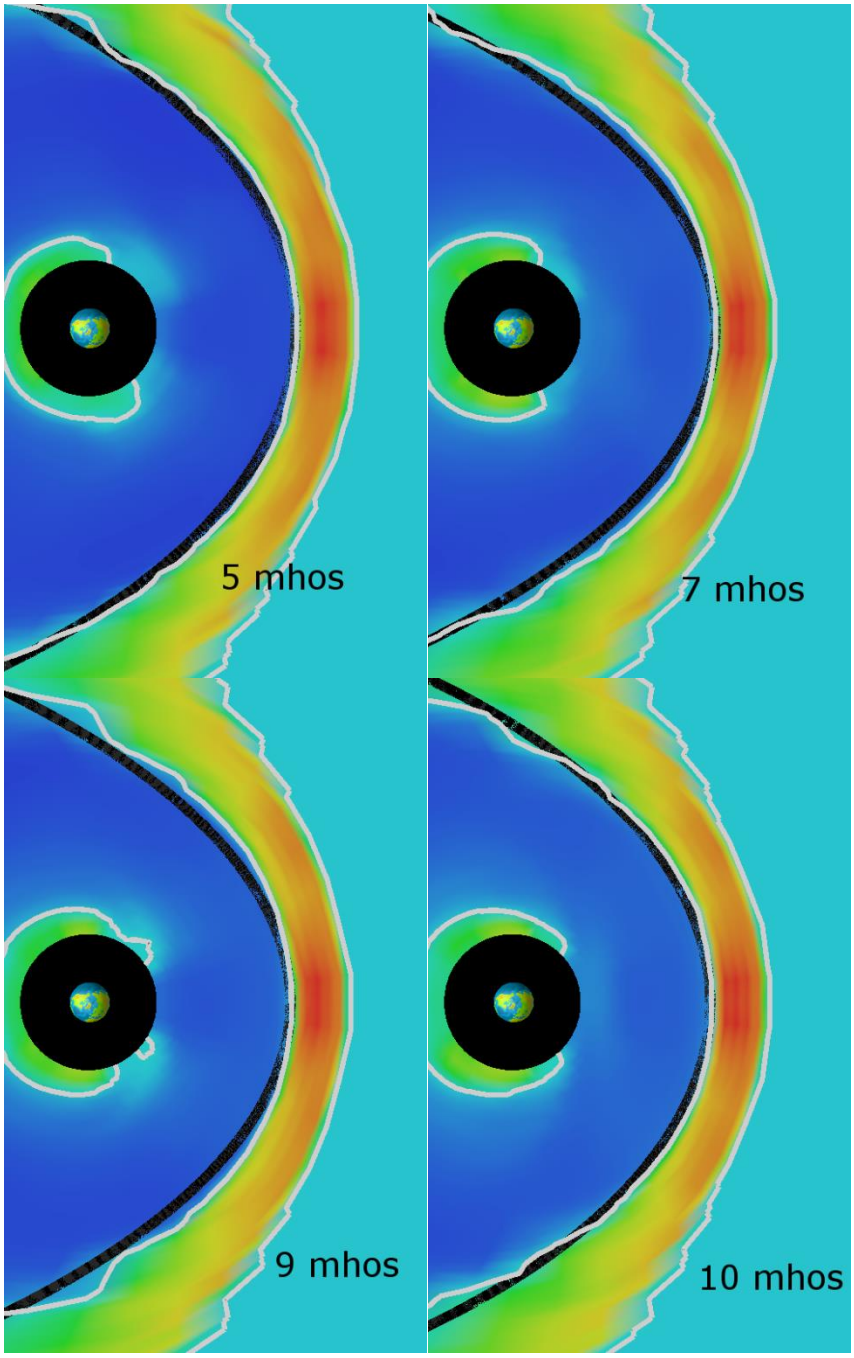

Figure 2.3 Magnetopause fits superimposed onto -1B_z LFM simulation results of different conductance.

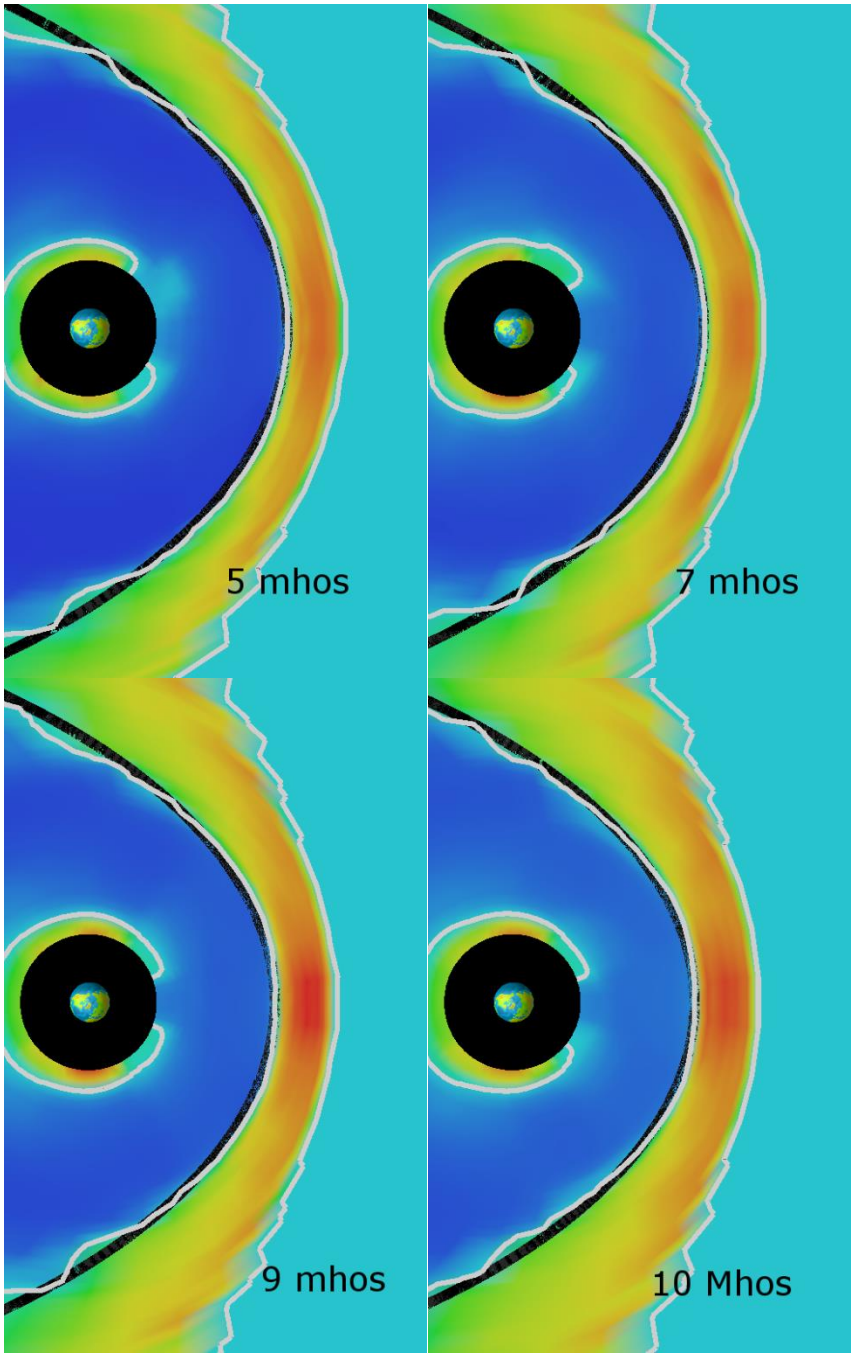

Figure 2.4 Magnetopause fits superimposed onto -3B_z LFM simulation results of different conductance.

Chapter 3

Whole Heliosphere Interval

The Whole Heliosphere Interval (WHI) is a period of time that was chosen to be the focus of an international effort by both the observation and simulation communities. This effort produced a special issue of the Journal of Atmospheric and Solar-Terrestrial Physics on CIR modeling of the WHI. The WHI corresponds to Carrington Rotation (one rotation of the Sun) 2068 which began on March 20 and extended through April 16, 2008. This period was during a time when the Sun is entering a deep solar minimum and, as described in previous sections, the dominant solar wind structures that create geomagnetic disturbances during solar minimum are CIRs and HSSs as opposed to the CMEs seen during solar maximum.

Figure 3.1 shows the solar wind OMNI data for the WHI. OMNI is a compilation of data taken by satellites located that the Earth's L1 Lagrange point. The data is then propagated to the nose of the Earth's bow shock such that the time component of the OMNI data set is what the solar wind would appear to be if we had a satellite measuring at the nose of the Earth's bow shock. We can see from the Figure 3.1 that each half of the WHI contains a CIR followed by a HSS. The compression caused by the HSS pushing on the slower solar wind in front of it can be located by a spike in density and a much more varied magnetic field. The rarefaction occurs during the HSS, which can be identified by both the low density and higher velocity. Comparisons made between observations and simulations are well documented [e.g., Wiltberger et al., 2012] and several studies simulated the WHI using LFM [Bruntz et al., 2012b; Lopez et al., 2012; Wiltberger et al., 2012]. These studies used the solar wind data shown in Figure 3.1 to drive the LFM simulation.

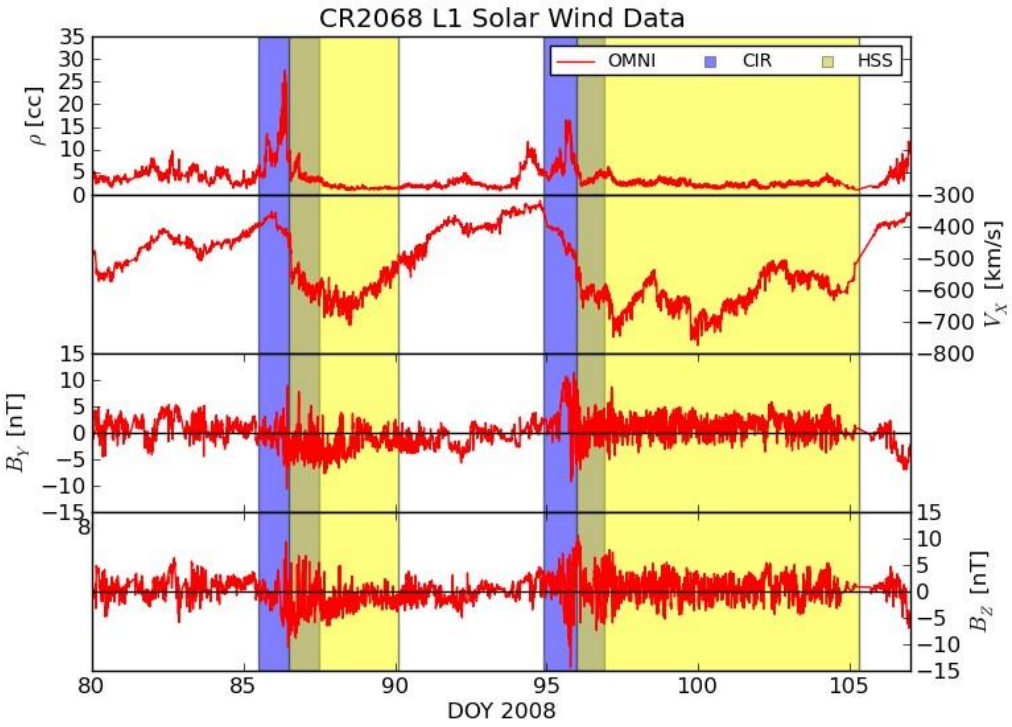

Figure 3.1 Solar wind measurements for the Whole Heliosphere Interval. [From Wiltberger et al., 2012]

Wiltberger et al. [2012] examined another Carrington rotation, in addition to the WHI, using the Coupled Magnetosphere Ionosphere Thermosphere (CMIT) model [Wiltberger et al., 2004; Wang et al., 2004], which is the LFM simulation coupled with an ionosphere-thermosphere model, specifically the Thermosphere-Ionosphere Nested Grid (TING) model. For each Carrington rotation, CMIT was driven using solar wind OMNI data, taken from satellite measurements at the L1 Lagrange point and propagated to the Earth's bow shock, and another CMIT run was done using solar wind data that comes from the output of a heliosphere-solar wind coupled model. These simulation results were then compared to a variety to satellite and ground-based observations.

It was concluded that when CMIT was driven with the solar wind from a heliosphere model, CMIT poorly replicate observations. The heliosphere model produced weak magnetic fields, the ultralow frequency waves that were present in the solar wind L1 data, were nonexistent in the heliosphere model output. This is not that surprising given the limited resolution of the solar wind model (the entire magnetosphere of the Earth fits in a single cell). Such a model simply cannot represent the observed variation of the IMF, which has a much smaller spatial scale. The small overall IMF means that the driving of the magnetosphere will be weak, and that quantities such as the ionospheric potential will be smaller than observed.

On the other hand, CMIT, when driven by the solar wind measured at L1, repeatedly provides values of the potential that are larger than observations, however, the overall development of activity remains close to that seen in observations during the entirety of the month-long simulation. Therefore, CMIT, driven by solar wind data taken at the L1 point, offers reasonably good representation of reality. This overestimation of the potential is due to the conductance being too low; discussed in the previous chapter. Wiltberger et al [2012] strongly suggests that this is directly related to weak electron precipitation power. The ionospheric model uses the electron precipitation as an input to the conductivity model, so an unrealistically low value of electron precipitation will cause the conductances to be too low and cause the potentials to be higher in response.

3.1 Viscous Potential during the WHI

For further testing of LFM's performance during the WHI, we benchmarked LFM's results against empirical formulas for the viscous potential [Bruntz et al., 2012a; Newell et al., 2008]. We do not have the capability of running the CMIT code locally so we instead ran the simulation using the standalone LFM code. The TING model that is

coupled LFM in CMIT provides more detail of the ionosphere than the empirical ionosphere employed by the standalone LFM. However, as we will see, the higher resolution ionosphere with more physics did not make a very large difference in global outputs such as the value of the ionospheric TPP. LFM was run with the full solar wind input file of the WHI and an F10.7 value of 74 SFU for the empirical ionosphere. An F10.7 value of 74 SFU is the average for the WHI interval.

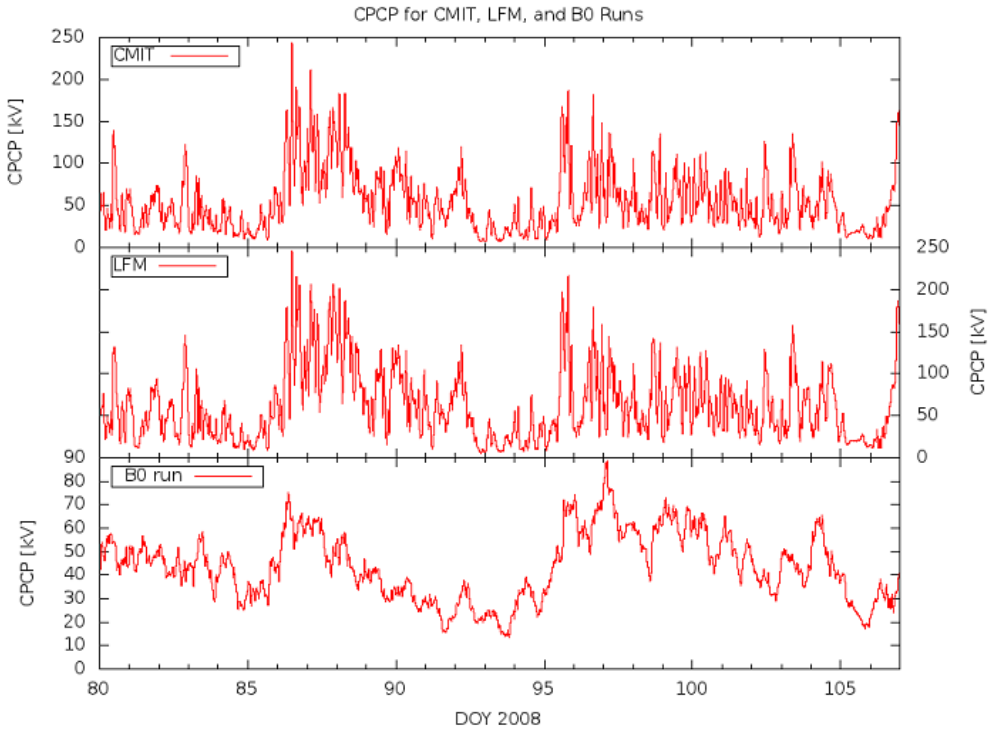

Figure 3.2 TPP results from CMIT, standalone LFM, and LFM run with zero IMF (B0 run). [Figure 3 from Bruntz et al., 2012b]

The top two plots in Figure 3.2 verifies that the standalone LFM and CMIT provide outputs that were almost the same. Verifying that the results are similar allows us to run multiple modified runs easily on local machines for this study. These results show that the essential physics are present in the standalone LFM and that nothing

significant is lost by running LFM instead of CMIT. On closer inspection of the TPP, the differences between the two results tended to be localized in some of the large TPP spikes. This is likely due to the fact that the TING model in CMIT has a more detailed ionosphere and therefore provides a slightly higher conductance than the empirical ionosphere in the standalone LFM.

In addition to running LFM driven by the solar wind with full IMF, we also ran LFM with solar wind input in which all of the IMF components in the WHI solar wind file was set to zero (leaving only the plasma timeseries). We call this run the B0 run. When there is no IMF present in the solar wind then no magnetic reconnection is occurring, resulting in a run in which the TPP is entirely the product of the viscous interaction. The TPP for this run is plotted in the third panel of Figure 3.2.

3.1.1 Viscous Potential Models

The B0 run produces a simulation where the resulting TPP is entirely due to the viscous interaction and can be compared to viscous potential models. In particular, we compared the B0 TPP to the Newell et al. [2008] viscous coupling term and the Bruntz et al [2012b] viscous potential formula. Newell et al. [2008] used 10 magnetospheric state variables as candidates for a best fit for the viscous and merging interactions from observational data. The best fit contained both a viscous coupling term and a merging term but we are interested in the resulting viscous coupling term, $n^{1/2}V^2$. The viscous coupling term describes how the viscous interaction couples with the solar wind density and velocity but does not directly compute a viscous potential.

Finding solar wind conditions that contain very little merging is difficult and greatly restricts the number of data sets obtained. MHD simulations, on the other hand, have no difficulties in generating a large data set of solar wind conditions in which no merging occurs. Bruntz et al. [2012a] used LFM to gather the viscous potential for

varying combinations of density and solar wind velocity. The resulting fit to this set of data gives the following formula to calculate the viscous potential: $\Phi_{BVP} = (0.00431)$ $n^{0.439}V^{1.33}$ for n in cm^{-3}, V in km/s and Φ_{BVP} in kV. We will refer to the Bruntz et al. [2012a] calculation of the viscous potential as the Bruntz potential or Bruntz viscous potential.

The Bruntz potential formula was created using LFM runs with a constant uniform ionosphere where the Pedersen conductance was 10mhos. As mentioned in the previous chapter, setting the Pedersen conductance to 10mhos provides realistic potentials; therefore the values obtained from the Bruntz potential should be representative of realistic values. The B0 run uses the empirical ionosphere model and produces unrealistically high potentials. We can apply a scaling factor, γ, to the TPP of the B0 run to match the B0 run to realistic values. This scaling factor is essentially correcting for the fact that the empirical ionosphere produces conductances that are too low.

The main difference between the Bruntz potential formula and the Newell et al. [2008] viscous coupling term is the lack of a constant in the latter. Following a method similar to Bruntz et al. [2012a], we apply a scaling factor to the viscous coupling term; resulting in the formula: $\Phi_{NVP} = v\, n^{1/2}V^2$ where v is a scaling factor and Φ_{NVP} is the Newell viscous potential or Newell potential. The magnitude and units of v are significantly different than the scaling factor of 0.00431 found for the Bruntz potential, due to the different powers applied to density and velocity in each formula. This scaling factor turns the Newell et al. [2008] viscous coupling function into a predictive formula for the viscous potential.

3.1.2 Solar Wind Delay

The Bruntz potential and Newell potentials take the solar wind density and velocity from the OMNI data set, where solar wind data has been propagated to the bow

shock, and then calculate a viscous potential. This type of calculation does not take into account any sort of time delay associated with the solar wind-magnetosphere interaction and will simply provide an instantaneous potential for a given density and velocity. Both the full run and the B0 run TPP values inherently have this time delay since they are based on the physical system. The solar wind data that are fed into the Bruntz potential formula and Newell potential formula have a 1-minute cadence.

The output from LFM is given in "time steps". Each time step does not necessarily correspond to the same amount of time, e.g. going from time step 250 to 500 may take 1.3 minutes while going from time step 500 to 750 may take 1.8 minutes. We fixed this by interpolating the TPP from the full run and the B0 run to every integer minute value. This allows us to do a direct minute by minute comparison between the simulation runs and the formulas. The Bruntz potential is adjusted by 1 minute intervals until we obtain the best correspondence between the Bruntz potential and the B0 run. We obtained approximately 52 minutes as the best time-shift to apply to the Bruntz potential and the Newell potential to properly align them with simulation results. This time shift represents the solar wind propagation time as well as time for the momentum transferred by the viscous interaction to appear as Birkeland current in the ionosphere.

3.2 Conductance Scaling Factors

To find the scaling factors ν and γ, we first must solve a dilemma. The formula for the Bruntz potential was derived by Bruntz et al. [2012a] using ideal solar wind velocity conditions containing purely V_x; therefore, $V = V_x = V_{total}$. While the Newell et al. [2008] viscous coupling term used V=V_{total} rather than V_x. This brings to question whether V should be V_{total} or V_x, which can be dramatically different due to contributions from V_y and V_z. To figure this out, we found 11 steady intervals throughout the WHI, to reduce

any noise introduced by fluctuating values, and calculate both the Bruntz potential and Newell potential using both V_{total} and V_x. These potentials are then plotted against the B0 run potentials. We initially chose a γ of 1.4 and ν of 8.92 x 10-5 to produce values approximately in the correct range. The choice of constants do not matter effect the plots, since they are constants. We can see from Figure 3.3 that the choice of Vx for both the Bruntz potential and Newell potential produces better results, an R^2 of approximately 0.91 for V_x and approximately 0.88 for V_{total}.

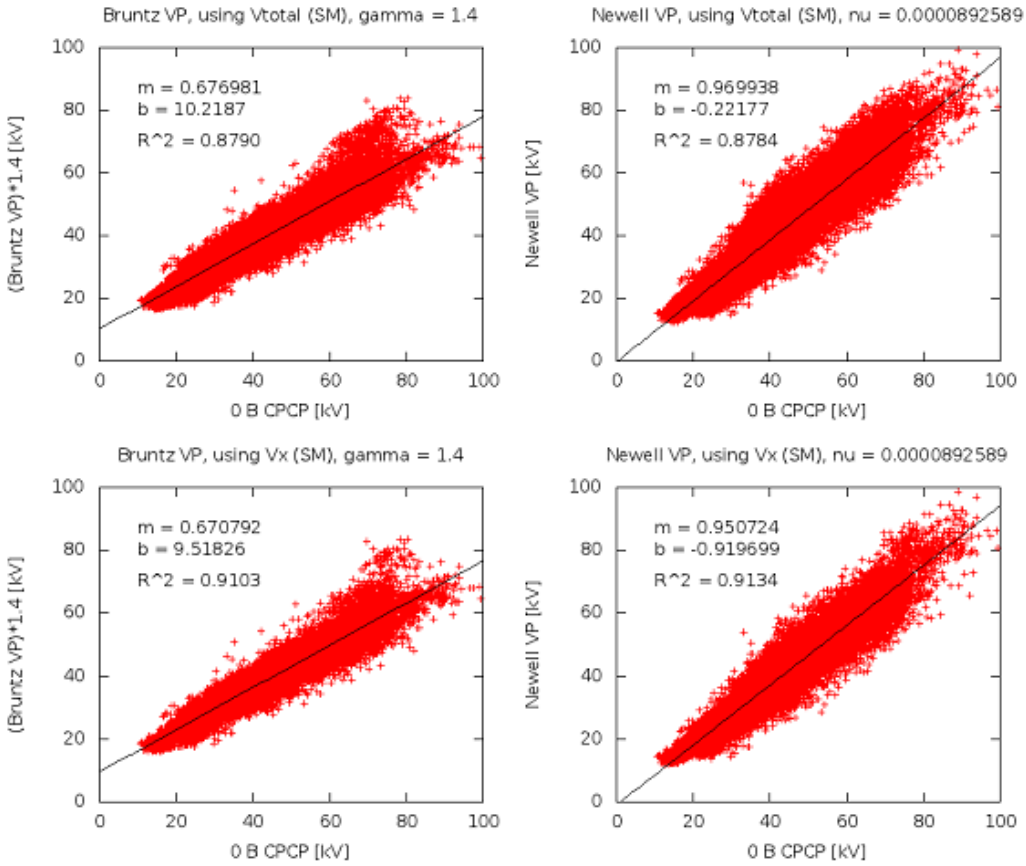

Figure 3.3 Potentials from Bruntz et al. and Newell et al. equations, using V_{total} and V_x as inputs, plotted against the potential from B0 run. [Figure 5 from Bruntz et al., 2012b]

We now know that V_x provides the better results. Given that there are four variables in calculating Bruntz potential and Newell potential, n, V_x, Φ, and their respective scaling factor γ or v, we can algebraically solve for the scaling factor by using the average n, V_x, and Φ from each of the 11 steady intervals previously used. This gives us a range of values for γ from 1.154 to 1.803 and a range of values for v from 5.816×10^{-5} to 7.419×10^{-5}. Since we are looking for a scaling factor that can be used across the entire WHI, we opted to use the average value for each; giving us $\gamma = 1.542$ and $v = 6.393 \times 10^{-5}$.

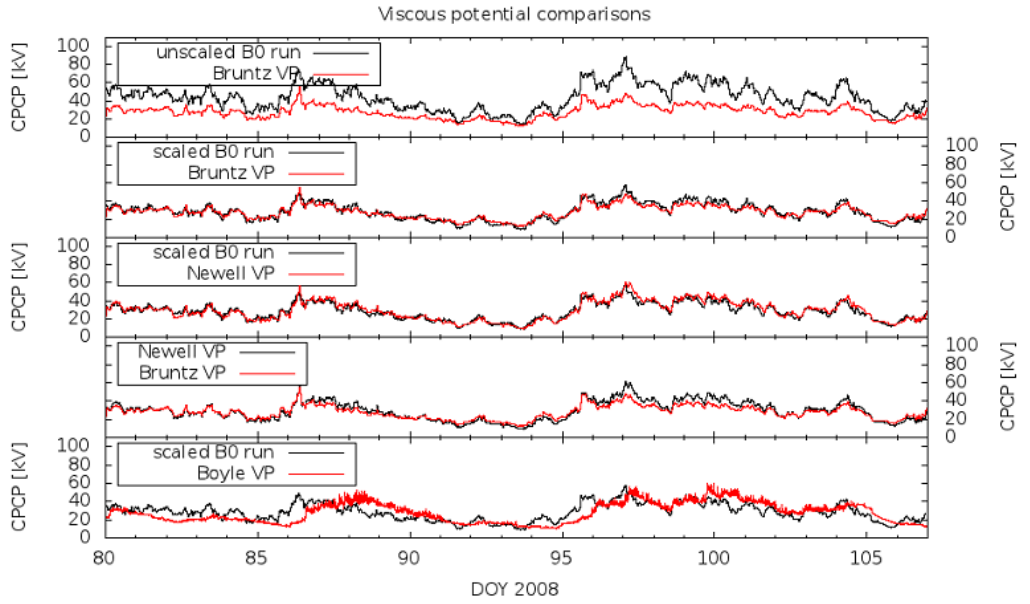

Figure 3.4 Plots of the B0 run TPP, Bruntz potential, Newell potential, and the Boyle et al. viscous potential. [Figure 6 from Bruntz et al., 2012b]

The γ scaling factor was applied to the B0 run to match the B0 run to realistic values and the v scaling factor was applied to the Newell et al. viscous function to produce a potential. The resulting potentials are plotted in Figure 3.4 as well as the viscous potential from Boyle et al. [1997] equation, which is simply: $\Phi_{Boyle} = 10^{-4}V^2$, where

$V = V_{total}$. It is immediately clear that the first panel in the figure, which is a comparison of the unscaled B0 TPP to the Bruntz potential, does not seem to agree very well but the second panel where the B0 TPP has now been scaled by the γ factor agrees exceptionally well. This is particularly surprising due to the fact that the Bruntz potential was developed using a series of steady state potentials with an idealized constant conductance ionosphere and not the empirical ionosphere. The third panel and fourth panel comparing the B0 TPP, Bruntz potential, and Newell potential all displays good agreement. Unsurprisingly, the simple formulation by Boyle et al. [1997] does not perform too well as it does not take into account density variations.

3.1.3 Comparisons to an Empirical Ionosphere Model

To fully understand the consequence of the conductance scaling factor, we compared the scaled and unscaled TPP from the full solar wind LFM run to the Weimer05 model [Weimer, 2005]. The Weimer05 model is an empirical ionospheric model that calculates electrodynamic properties of the high-latitude ionosphere and uses the Assimilative Mapping of Ionospheric Electrodynamics (AMIE) model [Richmond and Kamide, 1988; Ridley and Kihn, 2004] as the base of the model. It also uses the solar wind data as an input. Figure 3.5 overlays the unscaled full solar wind LFM TPP with the Weimer05 potentials in the first panel and the scaled LFM TPP with the Weimer05 potentials in the second panel.

Similar to Wiltberger et al. [2012], we found that LFM provided TPP that were consistently higher than the more realistic Weimer05 model. Interestingly, even though we know that the unscaled LFM TPP should give consistently larger than realistic values, the lows of the unscaled LFM TPP are lower than that produced by the Weimer05 model. Regardless of the solar wind driving conditions, the Weimer05 model never drops below a floor of ~ 25 kV that is built into the model. There is no hard floor or limit to the lowest

TPP that is obtainable by LFM. LFM simply produces a TPP value based on the given solar wind and ionospheric conditions.

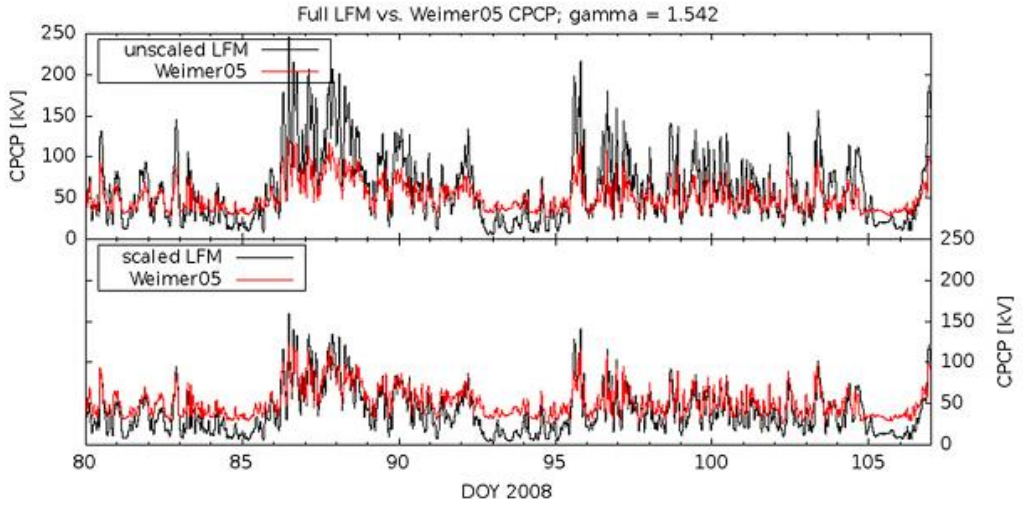

Figure 3.5 Comparison of the TPP from the full solar wind LFM (both unscaled and scaled by γ) and the Weimer [2005] model. [Figure 7 from Bruntz et al., 2012b]

Since the Weimer05 model is an empirical ionosphere, it is expected and known that the model generally produces realistic TPP values. To reduce the LFM TPP to more realistic values and possibly to levels similar to Weimer05, the LFM full solar wind TPP was also scaled by the same scaling factor that was developed for the B0 run in the previous sections. Ignoring the scaled LFM potentials that were already lower than the Weimer05 values, the scaled LFM potentials at higher TPP values show a surprisingly close agreement but not matching exactly.

This is a remarkable result since the γ scaling factor was created to scale results from a viscous only empirical ionosphere LFM run to match with results from uniform ionospheric conductance LFM runs. It implies that the scaling factor γ is correcting for some underlying issue and not simply a “fudge factor” that was developed to convert between different data sets. We reason that this supports the argument made by Wiltberger et al. [2012] that the ionospheric models employed by LFM are producing

conductances that are too low because they are not accounting for a sufficient amount of particle precipitation. The γ scaling factor seems to be correcting for some of these effects when applied to the simulation results.

3.2 Northward Bz and Reconnection Potential

An interesting feature emerges when the plots of the TPP from the B0 run and from the full run are overlaid. In Figure 3.6, we can see that there are periods in which the TPP from the full solar wind LFM run, and also CMIT, dips below the B0 run. The viscous potential gets reduced by the reverse convection cells present during periods of northward Bz [Bhattarai et al., 2012; Lopez et al., 2012]. With increasing northward Bz, the viscous potential will continue to decrease until the reconnection potential overtakes the viscous potential. Although no immediately clear, the periods where B0 is greater than the full solar wind run are periods where the IMF is northward [Lopez et al., 2012].

The explanation made by Lopez et al. [2012] is based on the different configurations of the transpolar potential distribution. During southward Bz, the idealized steady state polar cap only has two circulation cells. The viscous potential, for southward Bz, is constant and is weak in comparison to the reconnection potential [Bruntz et al., 2012a]. For there to only be two circulation cells seen, then the viscous is completely nested inside of the reconnection cell and the two potentials constructively add together, both adding to $\Phi_{measured} = \Phi_{max} - \Phi_{min}$, or for B_z to be equal to 0nT and purely viscous, shown in panel a of Figure 3.7.

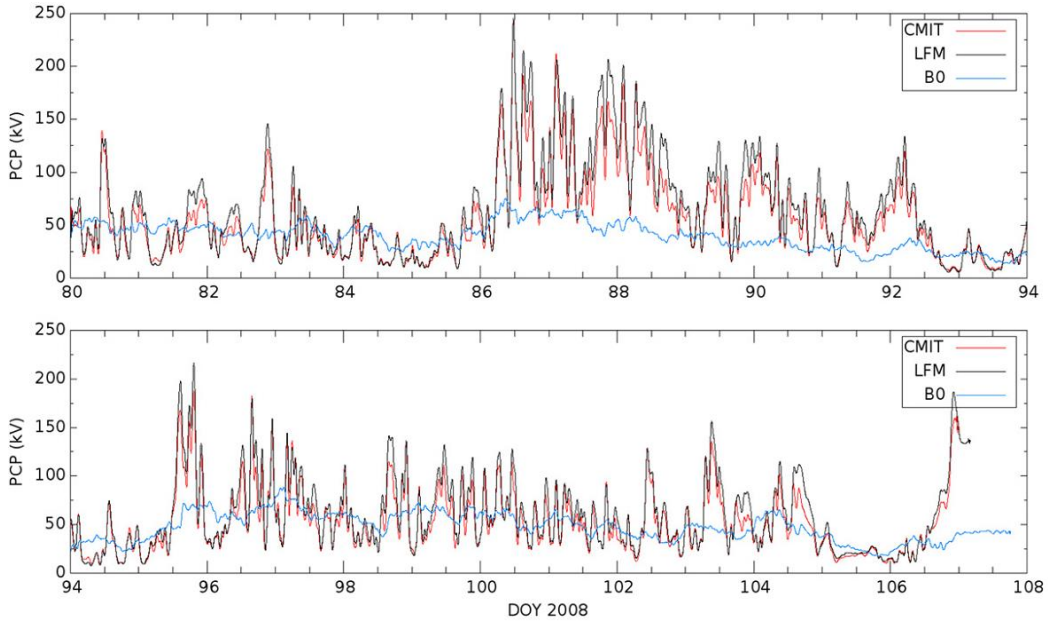

Figure 3.6 TPP for the LFM run with the full IMF, CMIT, and the LFM run with zero IMF. [Figure 2 from Lopez et al., 2012]

The polar cap configuration for northward B_z contains a four-cell pattern that do not add together like that seen for southward B_z [e.g. Burke et al., 1979]. At small values of northward B_z, two additional reverse convection cells appear at the very high latitudes (0 degrees latitude is roughly at the center of dusk and dawn). As seen in panel b of Figure 3.7, these reverse convection cells are still smaller than the viscous cells at lower latitudes and the measured TPP is entirely due to the viscous cells. When the magnitude of northward B_z becomes larger, the reverse convection cells start to grow in size seen in panel c but the cells are still smaller than the viscous cells. The resulting measured TPP is still the max minus the min of the viscous cells. Only when we reach even larger values of northward B_z, as shown in panel d, do the reverse connection cells overtake the viscous cells resulting in the measured TPP being the reverse convection cells. Unlike southward B_z, the measured TPP is not representative of both the reverse convection cells and the viscous cells but rather the greater of the two.

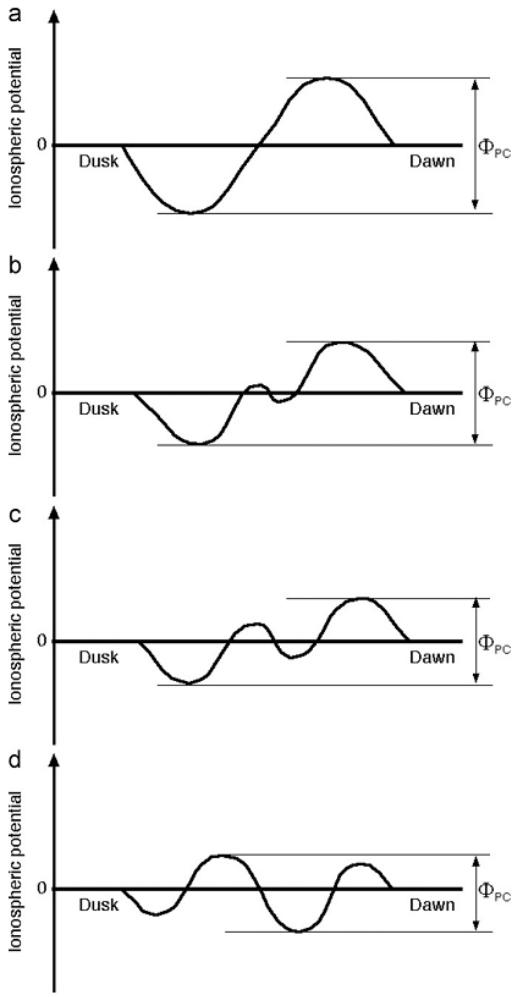

Figure 3.7 Schematic of the ionospheric potential minima and maxima for varying northward Bz; no IMF present (a), small values of Bz (b), larger northward Bz (c) and even larger northward Bz (d). [Figure 5 from Lopez et al., 2012]

3.3 Linear Separation of B_y and B_z

As seen in the previous section, separation of the viscous TPP and the reconnection TPP is complicated but doable. The viscous TPP is independent of the strength of the southward Bz while the reconnection potential is clearly dependent and the total TPP is the linear addition of both together. For northward Bz, the situation is more complex but both the viscous interaction and reconnection are separable. Both

Bruntz et al. [2012b] and Lopez et al. [2012] were able to separate the viscous interaction from the merging interaction, and study each separately. This motivated us to consider the question of whether the merging interactions of the individual merging components of the IMF themselves were linearly separable. To answer this question, we conducted numerical experiments to see if the B_y and the B_z merging interactions were also linearly separable.

In the above studies, we had "turned off" the IMF by setting all components of the IMF to zero while maintaining the density and velocities for the WHI. As an extension of the above B0 run, we simulated two additional LFM runs; one where the B_y was set to 0 while maintaining all other parameters unchanged, including B_z, and another one where the B_z was set to 0 while maintaining all other parameters unchanged, including B_y. These two runs are essentially simulations of the WHI with purely B_z and purely B_y, respectively.

If the solar wind-magnetosphere interaction is linearly separable, then the Birkeland current is produced by the viscous interaction, the merging interaction with B_y, and the merging interaction with B_z. When we perform the run in which there is only purely B_y, then the resulting Birkeland current contains the viscous interaction and the merging interaction due to B_y. Previous studies have indicated that the viscous interaction in LFM appears to be independent of B_y [Mitchell et al., 2010], therefore the viscous interaction in the purely B_y run is equal to the viscous interaction in the B0 run. The situation for the purely B_z run is slightly more complex. The viscous interaction also appears to be independent of negative B_z [Bruntz et al., 2012a] but positive B_z will affect the strength of the viscous interaction [Lopez et al., 2012; Bhattarai and Lopez, 2013].

The purely B_z run, $I_B(B_y = 0)$, contains both the merging interaction with B_z as well as the viscous interaction that is influenced by B_z. This means that the only thing missing

from the purely B_z run is the merging interaction with the B_y, to reconstruct the full solar wind run. Since the viscous interaction is independent of B_y, we can isolate the merging interaction with B_y by subtracting the B0 run, $I_B(B_{tot} = 0)$ from the purely B_y run, $I_B(B_z = 0)$.

If the interactions are indeed linearly separable, we should be able to reconstruct the Birkeland current for the whole run using the relation:

$$I_B(total) = I_B(B_y = 0) + I_B(B_z = 0) - I_B(B_{tot} = 0) \quad (3.1)$$

where the integrated Birkeland current for the full solar wind LFM run is denoted $I_B(total)$, $I_B(B_y=0)$ is the integrated Birkeland current for the run that contained purely B_z values and the B_y was set to zero, $I_B(B_z=0)$ is the integrated Birkeland current for the run containing purely B_y and the B_z was set to zero, and $I_B(B_{tot} = 0)$ is the integrated Birkeland current for the B0 run that was simulated at the start of this chapter when both the B_y and B_z values were set to zero.

3.3.1 Accuracy of Linear Combination

The integrated Birkeland current of the linear combination of the three runs is overlaid with the full solar wind run in Figure 3.8. The result is remarkable in that the reconstruction from three separate runs is nearly the exact same as the integrated Birkeland current from the full solar wind run, for the over 2 week interval plotted. There are some slight discrepancies at the lowest and highest values, but the overall reconstruction is spectacular. In fact, when this result was first produced, the initial assumption was that something had gone wrong and that something had been done incorrectly, resulting in overplotting two identical runs. But after checking all of the simulation inputs and output files very carefully, it was determined that this surprising result was, in fact, a true output of the LFM simulation.

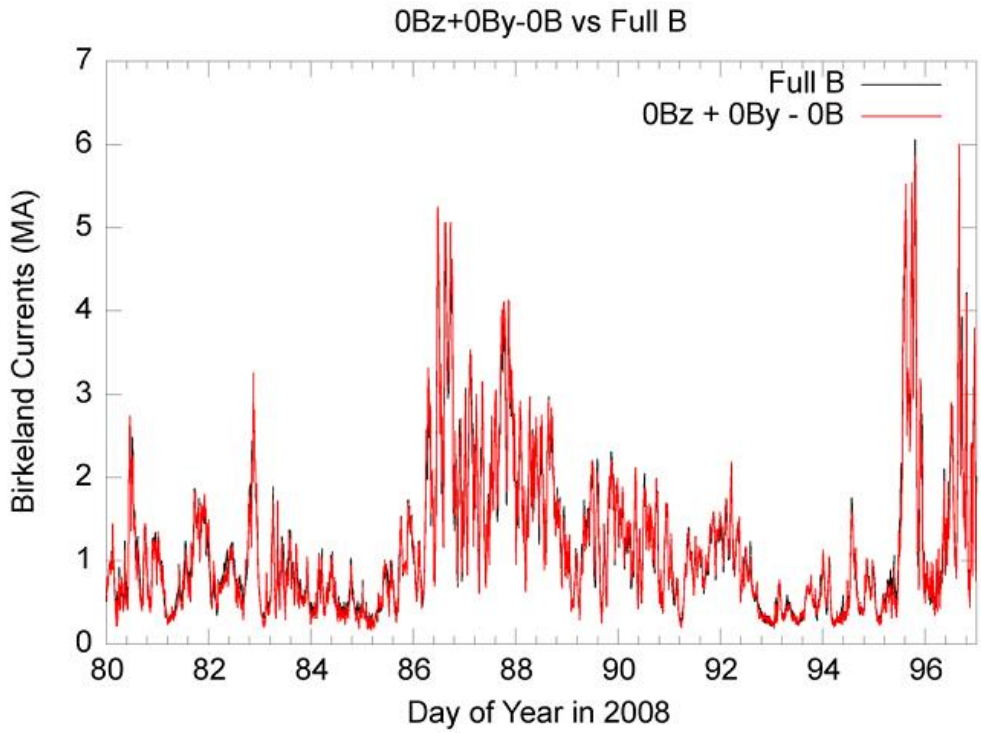

Figure 3.8 Comparison of the full solar wind run to the results of reconstructing the full solar wind from 3 separate runs [Figure 5 from Lopez et al., 2014].

Although equation (3.1) describes the relation for the Birkeland current, the same relation can be used for the TPP where I_B is replaced with Φ. We conducted the same comparison using the TPP instead of the I_B and arrived at similar picture and outcome seen in Figure 3.8. To better quantitatively understand the accuracy of the reconstruction, we plotted the linear combination of the three runs against the full solar wind run. We can see from Figure 3.9 that there is an exceptionally good correlation between the linearly reconstruction from three runs and the full solar wind run, $R^2 = 0.98$. There are periods in which there is a considerable amount of deviation between the two potentials and future work would pay special attention to these periods to determine under what conditions the linear superposition breaks down.

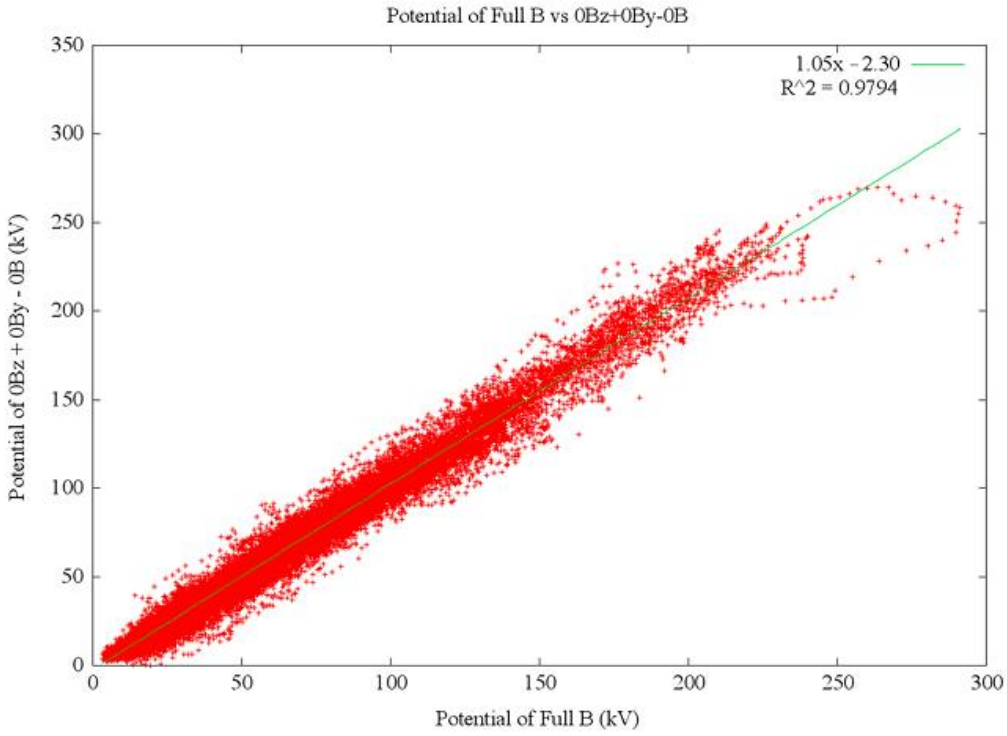

Figure 3.9 Comparison between the linear superposition of three simulation runs and the full solar wind run showing exceptionally good agreement.

3.3.2 Applications of Linearly Separable IMF Interactions

The ability to reconstruct the original full solar wind run using a linear superposition of three separate simulation runs is extraordinarily surprising and has some important implications. We showed at the start of this chapter that the TPP due to the viscous interaction can be modeled by using a viscous potential formula, for example the Bruntz viscous potential formula, with relatively good agreement to simulation. Taking the linear superposition one step further, we can replace the B0 run by the Bruntz potential and not have to run the B0 run in the first place. By extension, if formulas to describe the merging interactions with B_y and B_z, and a formula for the viscous potential during northward B_z were to be developed, then a good estimate of the TPP or I_B can be

calculated from simply using a linear superposition of these formulas. This would allow for near real-time approximation of the TPP and I_B for a given solar wind input without having to wait for simulations results.

Given the complex nature of the solar wind-magnetosphere interaction, it may not be entirely possible to formulate an accurate description for all the necessary components to create a fully mathematical expression for the TPP and IB. A second and possibly more viable application, would be to create a large dataset of solar wind conditions and to run the simulation ahead of time. Then for a given solar wind input, we could linearly combine the results that were already obtained in the dataset. The advantage would be that by using linear superposition in this way, all of the computation time has already been performed ahead of time; therefore, we would obtain a result at a fraction of the time it would have taken to run the MHD code with those conditions.

Chapter 4

Fluctuations in the Solar Wind

During solar minimum, the dominant solar phenomena are high speed streams (HSS) and their associated corotating interaction regions (CIR). The HSS typically contains a significant amount of Alfvénic oscillations in both the magnetic field and velocity. The Alfvénic oscillations are due to the presence of Alfvén waves in the solar wind but the solar wind itself can contain random fluctuations. In HSSs, the dominant type of fluctuations come from large amplitude Alfvén waves.

The large amplitude of the wave gives rise to large amplitude fluctuations that can cause solar wind that was previously southward (or northward) to become greater in magnitude or for weakly southward (or northward) to become northward (or southward). This enhancement of the magnetic field has been speculated to contribute significantly to the generation of geomagnetic storms that are caused by CIR/HSSs [e.g. Richardson, 2006; Tsurutani et al., 2006; Liemohn et al., 2010]. There are currently a lack of direct studies regarding the role that solar wind fluctuations play and so we seek to improve the understanding of solar wind fluctuations by exploring the amount of the energy deposited into the system by solar-wind-magnetosphere-ionosphere interactions with varying solar wind fluctuation amplitude.

As seen in the previous chapter, there are two CIRs/HSSs present in the WHI and each stream structure has a fluctuating magnetic field, as seen in Figure 3.1. The WHI has also been the focal point of intensive studies that have shown that simulation results are in good agreement with observation [e.g. Wiltberger et al., 2012]. This makes the WHI a prime candidate to be the benchmark for our series of numerical experiments that modify the solar wind fluctuations present in the WHI. By artificially modifying the

solar wind fluctuation amplitude, we can better understand and quantify the effects of the solar wind fluctuation amplitude on the solar-wind-magnetosphere-ionosphere interaction.

4.1 Solar Wind Fluctuations

We define the magnetic field fluctuations as the deviation of the magnetic field away from the baseline magnetic field; therefore the fluctuations can be isolated by subtracting out the baseline field from the original field. We start by finding the baseline magnetic field, which is the leftover magnetic field after all of the magnetic field fluctuations in the WHI are smeared out. This baseline magnetic field can be found by calculating a running boxcar average.

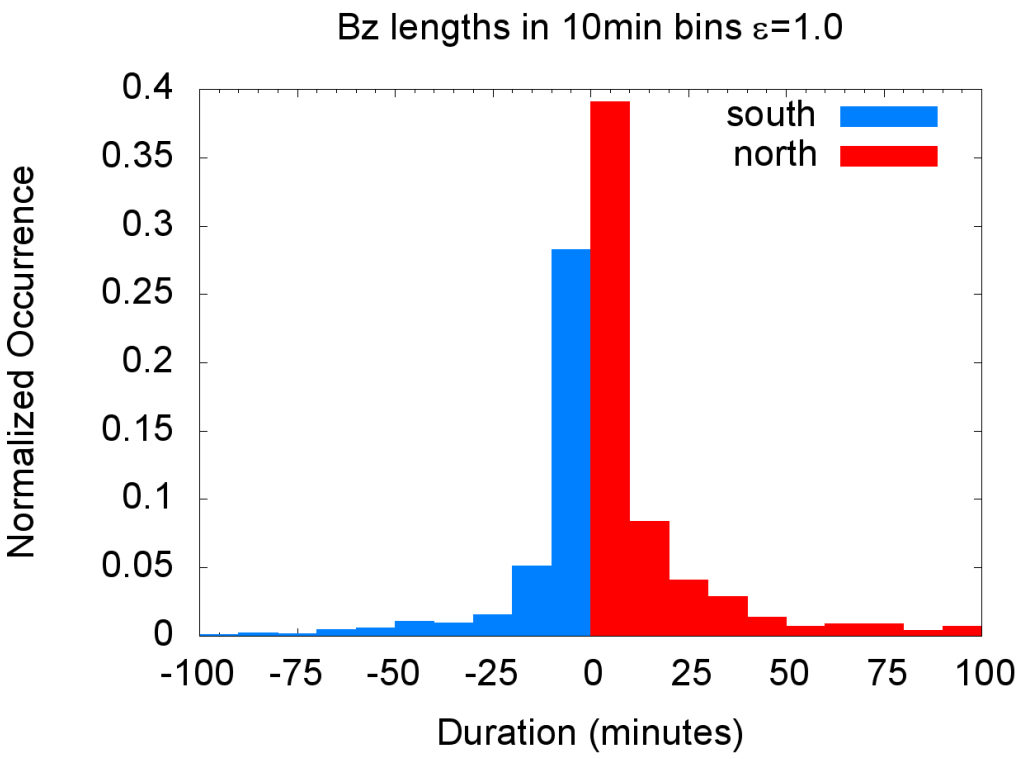

Figure 4.1 Normalized histogram of the duration of Bz before changing it changes signs [Figure from Pham et al., 2014].

To find an appropriate time length for the running boxcar average, we examine the duration of the periods of southward and northward. If the solar wind stays southward for 10 minutes, regardless of magnitude of Bz, before changing to northward, then we count that as a single southward event that lasted 10 minutes. We want the boxcar window to be sufficiently large to incorporate a majority of the solar wind fluctuations. From Figure 4.1, we can see that approximately 70% of the length of solar wind periods are under 10 minutes and approximately 95% are under 1 hour in length. A time length of under 1 hour is important, in that it does not allow for the ionosphere to approach the steady-state value and for the TPP to reach its optimal value for a given solar wind input.

A 4-hour interval was chosen for the running boxcar average because most of the fluctuations have a shorter period (so that we can average them out). This time period is also approximately the amount of time it takes LFM to reach steady state for a given constant solar wind input. The magnetic fluctuations, at a given time t_i, can be found using the equation:

$$\delta B_i = B_i - \langle B_i \rangle_{4hr} \tag{4.1}$$

where for direction component i, δB_i is the fluctuation amplitude, B_i is the value of the original field, and $\langle B_i \rangle_{4hr}$ is the running 4-hour box car average centered around time t_i. The same thing can be done to calculate the fluctuations in the Y and Z components of velocity. For the LFM simulation, we only consider the fluctuations in the Y and Z directions since the magnetic field in the x-direction is set to 0 for the simulation. Moreoever, it is the Y and Z components of the IMF that are geoeffective and that represent magnetohydromagnetic waves that are propagating outward from the Sun. The results of equation (4.1) allows us to calculate the fluctuations (δB_y, δB_z, δV_y, and δV_z) from the original fields (B_y, B_z, V_y, V_z).

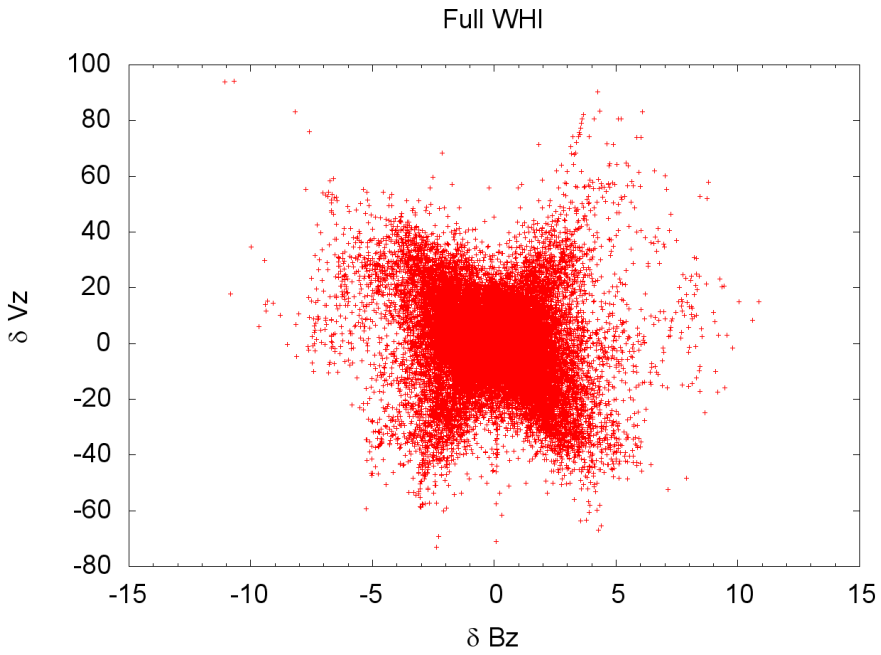

Figure 4.2 Scatter plot of the magnetic field and velocity perturbation for the WHI, showing a mix of both positive and negative correlation for the whole WHI [Figure from Pham et al., 2014]

To determine whether these fluctuations are primarily due to Alfvén waves, we use the fact that there is a correlation between the fluctuation in the magnetic field and the fluctuation in the velocity since Alfvén waves present in the solar wind will cause perturbations in both the solar wind magnetic field and the solar wind velocity. The scatter plot of δB_z and δV_z in Figure 4.2 shows that there is both a positive and negative correlation between δB_z and δV_z for the whole 27-day WHI. Since all waves are presumed to be propagating outwards from the Sun, then V_x will always be negative, and therefore, the sign of B_x will determine whether the correlation is negative or positive. Although not shown, the first CIR/HSS in the WHI contains both positively and negatively correlated fluctuations because of the varying sign of B_x. The second CIR/HSS, scatter plot in Figure 4.3, shows a clear predominance of negatively correlated Alfvén waves and

so for the purpose of this work, we will only conduct numerical experiments on the second half of the WHI. It has also been shown that simulations of the second CIR/HSS corresponded better with observations than the first CIR/HSS.

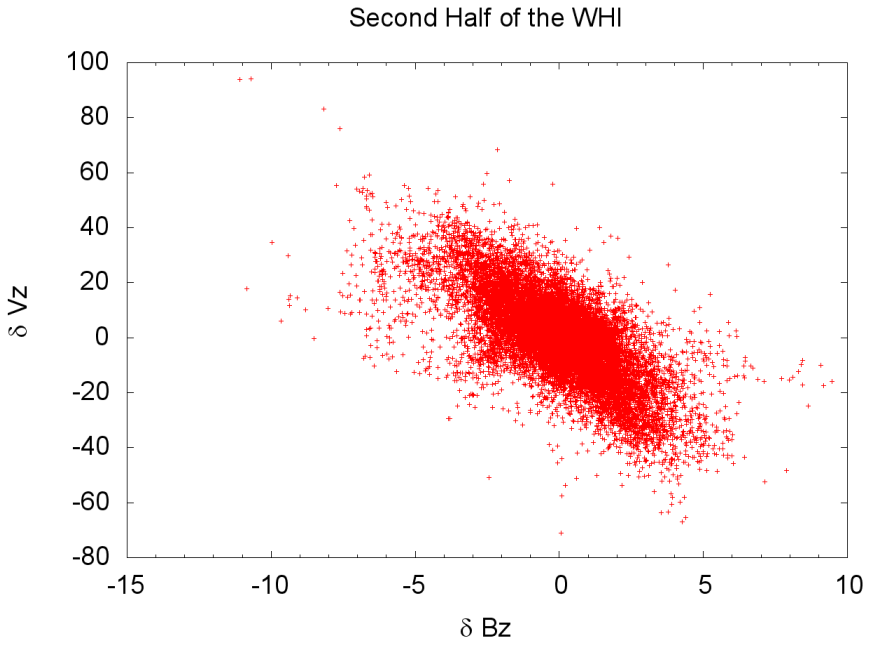

Figure 4.3 Scatter plot of magnetic field and velocity perturbation for the second half of the WHI [Figure from Pham et al., 2014]

Once the fluctuation has been separated from the baseline field, we can multiply the fluctuation amplitude by a scaling factor, α, before adding the fluctuation amplitude back to the baseline field. It follows that the original magnetic field B_i and the modulated magnetic field B_{mod} are associated by the relation:

$$B_{mod} = \langle B_i \rangle_{4hr} + \alpha * \delta B \tag{4.2}$$

where α is the fluctuation multiplier that allows for $B_{mod} = B_i$ when $\alpha = 1$. The velocity fluctuation amplitudes can be similarly modulated. To better understand the effect of

fluctuation amplitude on the solar wind-magnetosphere interaction, we simulate the second CIR/HSS using α = 0.5, 1, and 2.

4.2 Energy Transfer

A method of quantifying the effects of fluctuation amplitude on the solar wind-magnetosphere interaction is to examine the amount of energy deposited into the system by the solar wind and the amount of energy dissipated by the system. Since we are changing the input solar wind by modifying α, then both the energy deposited and energy dissipated are changing between each run. To better compare the runs, we will be calculating the efficiency of the energy transfer, η, of each run. The efficiency can be calculated by taking the ratio between total energy deposited and total energy dissipated for the entirety of each run.

4.2.1 Energy Input

Directly measuring or calculating the energy input is extremely difficult but we can estimate the energy input by using an energy function. There are several energy transfer functions that have been developed and we will use the most popular energy transfer function, specifically the energy transfer function developed by Perreault and Akasofu [1978], known as the ε parameter. The ε parameter, in watts, is given by the equation:

$$\varepsilon(W) = \frac{4\pi}{\mu_0} v B^2 \sin^4\left(\frac{\theta}{2}\right) l_0^2 \tag{4.3}$$

where μ_0 is the permeability of free space, v is the solar wind speed, B is the IMF magnetic field, θ is the IMF clock angle, and the factor l0 is an empirically determined scale factor with dimensions of length. Historically, this scale factor has been set to 7 R_E and corresponds roughly to the geoeffective length [e.g. Lopez et al., 2010], the window

in the solar wind in which all solar wind passing through this length will undergo magnetic reconnection.

As a first order approximation, ε(W) is a good estimate for the total energy input into the solar-wind-magnetosphere-ionosphere system. Under some conditions, complications arise in which the observed energy dissipated by the system was greater than ε(W) could account for, which is an unrealistic situation [Koskinen and Tanskanen, 2002]. It was concluded although the assumptions and formulation of ε(W) is relatively sound, a static scaling factor of 7 R_E may be the reason for why ε(W) has this dilemma. Several attempts to vary the scale factor, for example, Monreal-MacMahon and Gonzalez [1997] have made a correction to ε(W) by taking into account the magnetopause position and scaled the scaling factor according to the equation for the subsolar point found in Chapter 1. Another attempt was made by correcting for the solar wind ram pressure on the efficiency of the rate of magnetic reconnection [De Lucas et al., 2007]. Although both of these corrections provided the necessary factor to resolve the Koskinen and Tanskanen [2002] dilemma, its accuracy and precision have not been proven. For this study, we used the original ε(W) and the widely accepted scaling factor of 7 R_E.

4.2.2 Energy Efficiency and Dissipation

To get a good measure of the role that fluctuation amplitude plays in solar-wind-magnetosphere-ionosphere coupling, we compare the geoeffectiveness of each CIR/HSS simulated. The geoeffectiveness, or relative efficiency η, can be calculated by finding the ratio of the solar wind energy input, which is estimated by ε(W) for our study, and the energy dissipated by various energy sinks. When estimating the geoeffectiveness of geomagnetic storms, the ring current is commonly identified as the primary energy sink but, more recently, there have been studies that found that the ionospheric joule heating

can be a larger energy sink than the ring current [e.g. Lu et al., 1998; Knipp et al., 1998; Baker et al., 2001; Kane 2010; Guo et al., 2011].

The ring current itself naturally dissipates energy. Any deviation from the natural rate of dissipation means that there is an injection of energy into the ring current that the ring current must also dissipate away. The power dissipated by the ring current may be estimated by:

$$K\left(\frac{Dst^{PC}}{\tau} + \frac{\partial Dst^{PC}}{\partial \tau}\right) \tag{4.4}$$

where K=4x10^{13} joules/nT, DST^{PC} is the pressure-corrected *Dst* index values [Akasofu, 1981; Zwickl et al., 1987], and τ is the ring current decay time, which is taken to be six hours. *Dst* is an index of geomagnetic activity that is derived from magnetometers that are located near the Earth's equator and measures the intensity of the ring current. When the solar wind pressure is increased, then the magnetosphere becomes more compressed and so the ring current will naturally increase in strength. This is taken into account when we use the pressure-corrected *Dst* values, which can be calculating using the equations:

$$Dst^{PC} = Dst - b\sqrt{P_{SW}} + c \tag{4.5}$$

$$P_{SW} = 1.6727 * 10^{-6} * n * V^2 \tag{4.6}$$

where b = 7.26nT(nPa)$^{-1/2}$, c = 11.0nT, P_{SW} is the solar wind dynamic pressure given in nPA, n is the solar wind density given in particles per cc, and V is the solar wind velocity given in km/s [Burton et al., 1975; O'Brien and McPherron, 2000].

The other primary energy sink is the ionospheric joule heating. Joule heating is when energetic ions in the thermosphere and in the high-latitude ionosphere collide with neutral particles. The collision with the neutral particles will convert the energy of the moving ions into thermal and kinetic energy of the neutrals. This phenomena is similar to

the passage of electric currents through a conductor, which causes the conductor to release heat. For the LFM simulation, Joule heating can be calculated using the equation:

$$\vec{J} \cdot \vec{E} = \int \sigma_{Pedersen} * \left(\nabla(\Phi) \cdot \nabla(\Phi)\right) dA \quad (4.7)$$

where J · E is the ionosphere Joule heating, $\sigma_{Pedersen}$ is the Pedersen conductivity, and ∇Φ is the electric field , or gradient of the electrostatic potential. Calculating and integrating across the polar cap to calculate the Joule heating using equation (4.7) is not feasible for the real Earth's polar cap but the observed Joule heating can be quickly estimated by using the AE index. The Auroral Electrojet (AE) index is derived from perturbations in the horizontal component of the geomagnetic field observed from ground-based magnetometers located in the auroral zone in the northern hemisphere. From the work of Baumjohann and Kamide [1984], we can estimated the ionospheric Joule heating in the ionosphere in units of GW*hr by multiplying, 0.3*AE for the provisional hourly AE.

For our event of the second half of the WHI, the resulting energy dissipated by the ring current and by the ionospheric Joule heating in the northern hemisphere are 24 PJ and 168 PJ, respectively. Although both methods provide a crude estimate of the energy dissipated, they are not incredibly far away from actual values. In this case, the ionospheric Joule heating dissipates a significantly greater amount of energy than the ring current. The ring current only dissipated approximately 14% of the energy dissipated by ionospheric Joule heating in only the northern hemisphere. Since AE is only given for the northern hemisphere and the fact that the WHI is near equinox, then the energy energy dissipation between the north and south hemispheres are likely to be about the same. So the ring current contributes less than 10% of the global energy dissipated. This supports the previous studies that have found that the ionospheric Joule heating can

be a greater energy sink than the ring current, and it certainly is the case for our event. Although the LFM simulation does not contain any inner magnetospheric drift physics and therefore does not develop a significant ring current, this does not cause any problems as the Joule heating from the LFM ionosphere can be used to see the response of the system to the changes in the solar wind inputs.

4.2.3 Fluctuation Numerical Experimental Results

When the fluctuation amplitude is effectively halved or doubled, it is reflected in the ionospheric Joule Heating. Figure 4.4 shows an example of the ionospheric Joule heating over 2 days out of the 11 day simulation. It provides a snapshot of what happens when α is increased; almost all of the peaks are also increased but the troughs show a little difference picture. There are periods, for example between DOY 95 and 95.5, when $\alpha = 0.5$ and $\alpha = 1$ are at a very low point, $\alpha = 2$ peaks up but there are also periods, for example between DOY 95.5 and 96, when $\alpha = 0.5$ and $\alpha = 1$ reach a minimal value, $\alpha = 2$ appears to continue to drop even lower. We suspect that the solar wind between DOY 95 and 95.5 are when $\alpha = 1$ is weakly northward B_z and so when the fluctuations are increased to $\alpha = 2$, some of the weakly northward periods change to southward. During the periods between DOY 95.5 and 96, it is likely that periods that were weakly southward B_z became northward or if it was already northward and became even more strongly northward.

Similar to what is seen in Figure 4.4, Table 4.1 shows that as α increases the total energy input and out increases as well. These total energies are calculated by integrating the energy over the entire run. The increased fluctuation amplitude at $\alpha = 2$ causes southward B_z excursions to increase in magnitude and enhance the merging interaction, resulting in more energy transferred. Also, having more energy being transferred into the system means that as a result, more energy must also be dissipated.

The surprising result is the decrease in efficiency as the fluctuation amplitudes are increased from $\alpha = 0.5$ to $\alpha = 2$. A decrease in efficiency means that more energy must be added into the system to obtain an increase in energy dissipation.

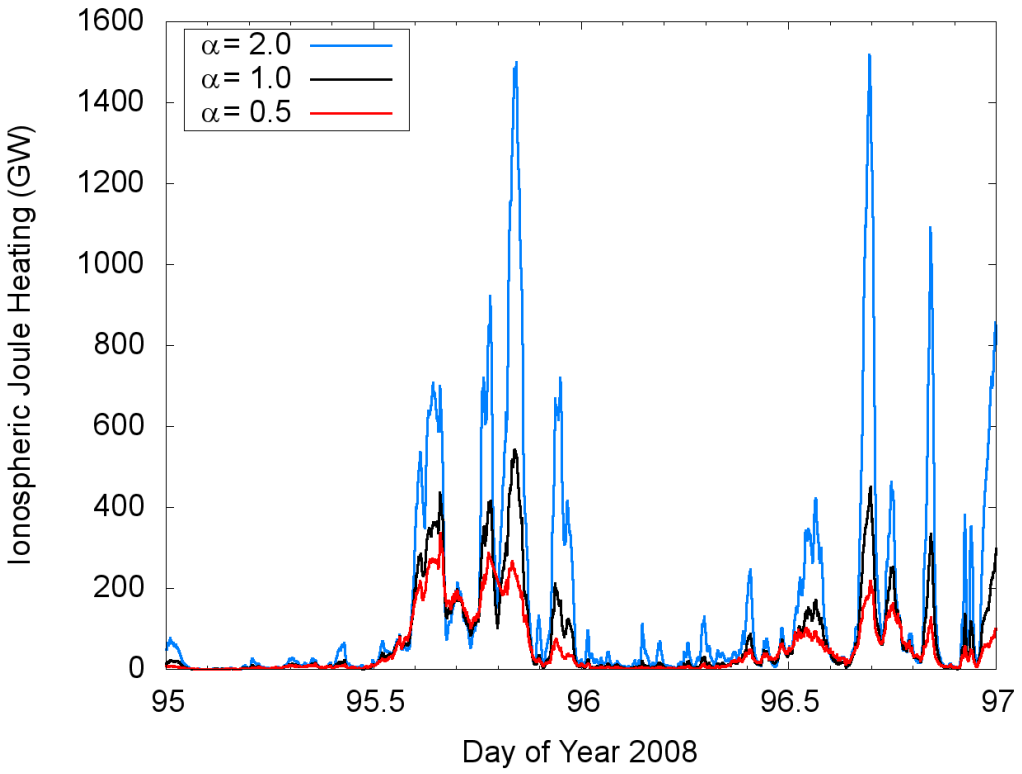

Figure 4.4 The ionospheric Joule heating from the LFM simulation for half the fluctuation amplitude ($\alpha = 0.5$), original amplitude ($\alpha = 1$), and doubled amplitude ($\alpha = 2$) [Figure from Pham et al., 2014].

Decreases in the efficiency with increasing fluctuation amplitude could possibly stem from a variety of factors. The method used to modulate the fluctuation amplitude changes the magnetic field (B_y and B_z) and velocity (V_y and V_z). However, the magnitude of the V_y and V_z are an order of magnitude smaller than the V_x. Although the changes to the velocity will certainly affect the viscous interaction, it is unlikely that increasing the fluctuation amplitude in Vy or Vz would change the viscous interaction by a sufficient

amount to result in the reduction in efficiency on the order that we saw from Table 4.1. We suspect that the decrease in η is due to the increased northward B_z presence.

Table 4.1 Total energy input (ε), total energy dissipated (Joule heating), and efficiency for varying fluctuation amplitudes. [Table from Pham et al., 2014]

Fluctuation Amplitude Multiplier	Total ε (PJ)	Total Joule Heating (PJ)	Efficiency η
α = 0.5	17.5	25.5	1.46
α = 1	33.2	35.8	1.08
α = 2	98.7	74.6	0.76

4.3 Reduction in Efficiency

We explore the possibility of the northward B_z affecting the efficiency of the southward B_z by performing a simple numerical experiment. LFM was ran using idealized conditions where V_x was -400km/s, V_z and V_y were 0 km/s, density was 5 particles cm^{-3}, B_x and B_y were 0 nT, and the F10.7 flux was set to the value used in the WHI (74 SFU). The idealized LFM simulation was initialized with 4 hours of B_z = -5nT to "empty" the magnetosphere of plasma through reconnection followed by 4 hours of B_z=+5nT to "load" the magnetosphere with plasma. At the 8th hour, B_z was changed back to -5 nT for two more hours before we introduced a northward turning that lasted for 20 minutes before changing back to a steady -5 nT.

4.3.1 Idealized Northward Turning

The top panel in Figure 4.5 shows the solar wind IMF for various northward turning values which have been lagged to account for the time it takes for the IMF to propagate through the system. The lag makes the northward turning line up with the impact seen in the ionosphere. Starting at a B_z value of 3nT for the northward turning, we incremented the northward turning B_z value by 1 nT for each successive run while all other conditions are maintained between the runs. We can clearly see the affect that the

northward turning has on the ionosphere in the last 3 panels inFigure 4.5. The TPP, integrated Birkeland currents, and the ionospheric Joule heating all immediately start dropping during the northward turning and drops to a lower value for larger northward IMF. Interestingly, it takes all of the outputs about 50 minutes to an hour to reach the fairly steady value held prior to the northward turning. Since it takes a finite amount of time for the potential to build up to steady state values [e.g., Lopez et al., 1999], the short period of northward B_z causes the ionosphere to weaken for a greater amount of time than the duration of the introduced turning.

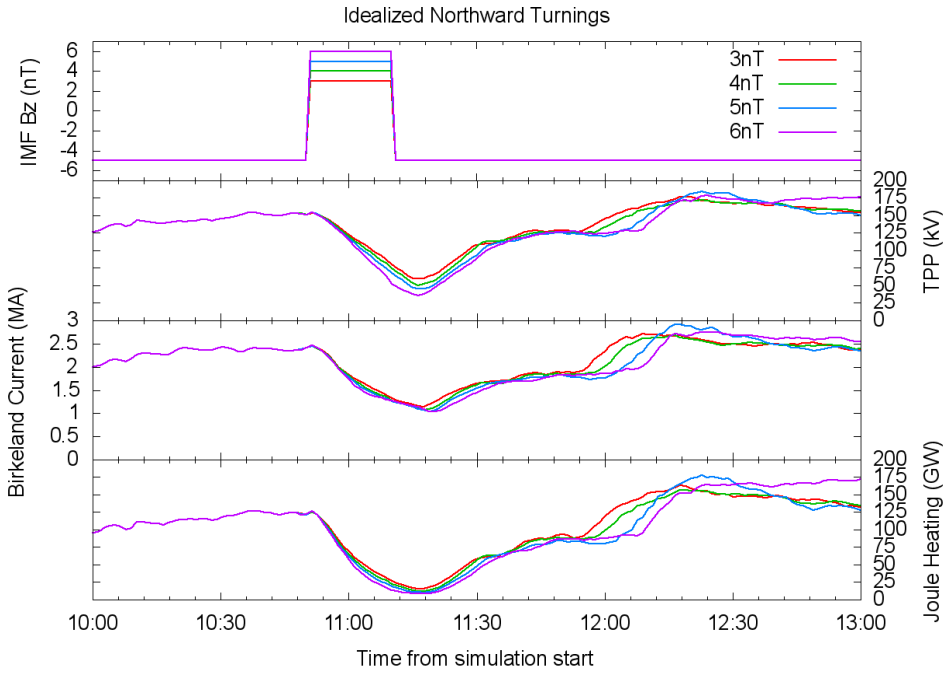

Figure 4.5 The lagged solar wind IMF and various ionospheric outputs for the set of simulations using idealized conditions and a northward turning occurring at 10:50 simulation time.

To better quantify the lasting effect of the northward B_z turning on the solar wind-magnetosphere-ionosphere coupling, we compared the energy and efficiencies in a similar manner done for the different α. Since the solar wind IMF after the northward

turning is back to a steady -5 nT, the input energy as defined by ε remains the same for all runs. Table 2.1 provides the ionospheric results for the hour following the northward turning. It is immediately clear that all ionospheric values (total Joule heating, average TPP, and average integrated Birkeland current) decrease with increasingly larger values for the northward turning. Since the total Joule heating decreases with larger northward fields but the input energy remains constant, then the resulting efficiency must also decrease when the value of the northward turning is increased.

Although the numerical experiment used a 20-minute duration for the northward turning, this duration is representative of the length of solar wind B_z intervals in the original WHI. As previously seen in Figure 4.1, the solar wind rarely extend beyond a 20 minute duration, therefore the results from Figure 4.5 and Table 4.2 have a major effect on the solar wind-magnetosphere-ionosphere coupling for our WHI event. We infer that when we increase the fluctuation amplitude, there will be both more and also larger northward turning occurring which will cause the ionosphere to be in a reduced state of energy dissipation for over an hour afterwards and, as a consequence, reduce the efficiency of the southward B_z periods.

Table 4.2 Results for the hour immediately following the northward turning [Table from Pham et al., 2014].

Max Northward Turning	Total ε (TJ)	Total Joule Heating (TJ)	Efficiency η	Average TPP (kV)	Average Integrated Birkeland Current (MA)
3nT	71.60	34.6	0.48	131	2.04
4nT	71.60	32.1	0.45	126	1.95
5nT	71.60	29.6	0.41	120	1.88
6nT	71.60	28.1	0.39	117	1.80

4.3.2 Other Sources of Efficiency Reduction

Although the numerical experiment helped to explain the reduction of the geoeffectiveness that was seen when α was increased, there may be potentially other sources that would decrease the efficiency and must also be considered. One possible factor is the saturation of the TPP [e.g., Lopez et al., 2010 and references therein]. Saturation takes place when the solar wind flow has a low Alfvén Mach number (less than 3.5) for an extended period of time. The Alfvén Mach number can be found using the equation:

$$M_A = V\frac{\sqrt{n}}{20B} \tag{4.8}$$

where M_A is the Alfvén Mach number, V is the magnitude of the solar wind velocity, n is the solar wind density, and B is the solar wind magnetic field. When α is increased, the fluctuation amplitude may increase the magnetic field to a large enough value for the Alfvén Mach number to be low enough to be in the saturation regime. If the solar wind IMF were large enough southward to be in the saturation regime then the ionosphere would not respond linearly to increases in southward IMF. A distribution of the Alfvén Mach numbers for the three α's can be found in Figure 4.6. Although α = 2 had significantly more periods of low Mach numbers, the periods corresponding to very low Mach numbers only accounted for a few percent of the total time and therefore had a relatively small, if any, impact on the overall efficiency.

Another possibility is that the increase in the fluctuation amplitude of B_y could affect overall efficiency. As previously found in Chapter 3, B_y and B_z are linearly separable and therefore any contributions to the efficiency from B_y or B_z are independent of each other. Since the processes that affect B_y are similar to the processes that affect B_z, the conclusions that were found B_z apply to B_y as well. The B_y field is neither steady

enough to reach a steady-state TPP to decrease the efficiency, nor is the B_y field large enough to be in the saturation regime. Therefore, B_y does not contribute to the reduction in the efficiency of energy transfer.

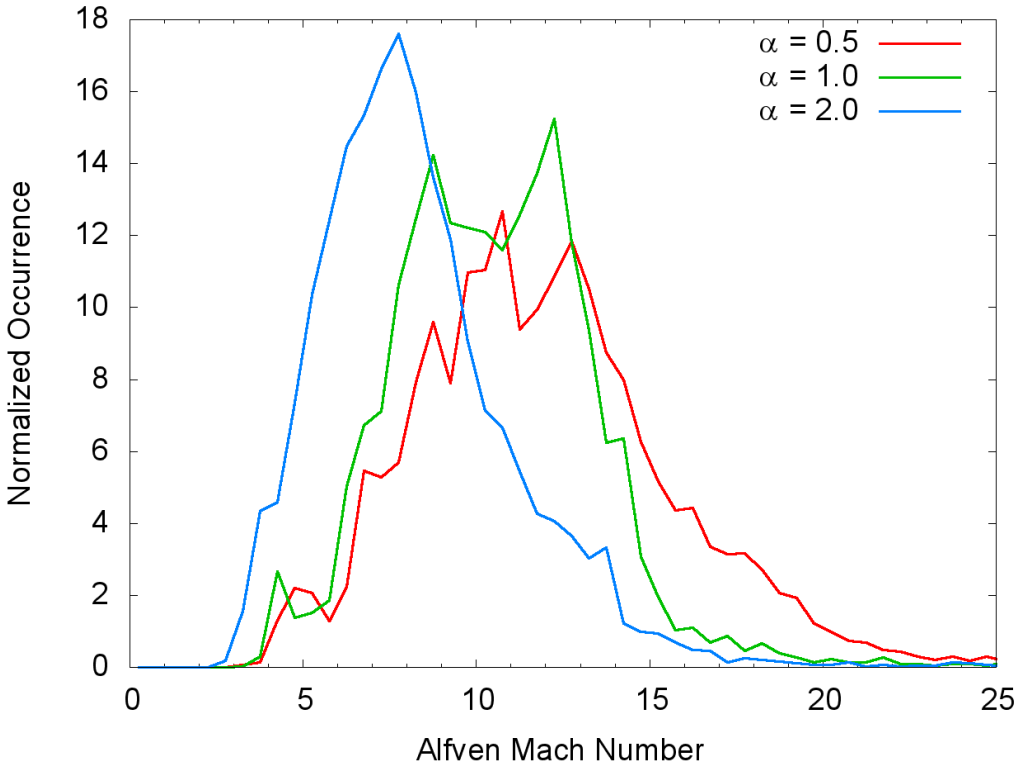

Figure 4.6 Distribution of Alfvén Mach number for the different WHI runs.

There is also the question of whether it is the presence of any fluctuation, rather than specifically northward IMF, that is causing the reduction in efficiency. To investigate whether southward fluctuations can contributing to the decreased efficiency, we perform an additional numerical experiment based on the WHI solar wind conditions. We set the solar wind B_z component to 0 nT every time the magnetic field is northward, or positive, and creating a southward-only WHI run. This modification was made to all 3 values of α and the results are shown in table blah. Compared to the runs with the full IMF enabled,

the total ionospheric Joule heating is dissipating at least 30% more energy for the southward-only runs. Although there is still a tendency for the efficiency to decrease with larger fluctuation amplitude, the change between $\alpha = 0.5$ and $\alpha = 2$ is much smaller than that seen for the full IMF run in Table 4.3. This suggests that the merging interaction that is being turned off, when B_z is 0 nT, is also causing a similar effect seen by the northward IMF. When the merging interaction gets turned off at $B_z = 0$ nT then turned back on when B_z is southward, the ionosphere will require additional time to build back up to its prior values similar to what was seen in the northward turning experiment.

Table 4.3 Total energy input, output and efficiency for the southward-only WHI run and amount of low Alfvén Mach number for the run.

Fluctuation Amplitude Multiplier	Total ε (PJ)	Total Joule Heating (PJ)	Efficiency η	Low Alfvén Mach Number (%)
$\alpha = 0.5$	21.7	34.8	1.60	0.1
$\alpha = 1$	40.2	49.5	1.23	0.16
$\alpha = 2$	115	101	0.88	3.0

After examining possible explanations for the decrease in efficiency with increasing fluctuation amplitude, we are left with our original explanation; that the increased presence, in both frequency and magnitude, of northward IMF is reducing the ionosphere's ability to efficiently transfer energy. While the total energy dissipation and ionospheric outputs are increased for larger fluctuation amplitudes, the geoeffectiveness decreases. The argument that the northward IMF is reducing the state of energy dissipation for an extended period of time after the magnetic field has returned from northward B_z to southward B_z is well supported by our numerical experiments.

Chapter 5

Conclusions and Future Work

5.1 Conclusions

The solar wind constantly flowing out from the Sun contain a number of magnetohydrodynamic waves that cause perturbations in the density, velocity, and magnetic field embedded in the solar wind. As the solar wind flows past the Earth and interact with the Earth's magnetosphere, large perturbations or fluctuations will propagate throughout the system and effect the solar wind-magnetosphere-ionosphere coupling. Studying the effect of large fluctuations directly is incredibly difficult. It is impossible to control the Sun to obtain multiple events with the same conditions but varying level of fluctuations in order to isolate the effects due to the fluctuations. Alternatively, computer simulations can be driven using a wide array of conditions, real or synthetic, and provide a level of spatial and temporal resolution of the magnetosphere that cannot be mimicked by satellite observation.

We used the Lyon-Fedder-Mobarry (LFM) global 3D magnetohydrodynamic simulation to study the geospace response to solar wind high speed streams that contain large amplitude fluctuations and the ionospheric response to different conductivities. We ran the simulation using a typical solar wind conditions (V_x = -400 km/s, density = 5 particles cm^{-3}), a B_z of -1 nT and -3 nT, and all other components are set to zero. Multiple runs were done each with a different ionospheric Pedersen conductance between 5 mhos through 10 mhos. The ionospheric Pedersen conductance regulates the current system in the magnetosphere and changes the shape of the magnetopause. By comparing the simulation magnetopause with the Sibeck et al. [1998] empirical magnetopause fit, we determined that the ionospheric Pedersen conductance at 10 mhos provided a more realistic magnetopause than 5 mhos. This supports the argument made

by Wiltberger et al. [2012] that the LFM simulation underrepresents the electron precipitation, therefore provides conductance that are too low.

We also looked at the geospace response of LFM during the Whole Heliosphere Interval (WHI), which was March 20 – April 16, 2008 (DOY 80-107). The ionosphere was driven with the average F10.7 for the WHI, of 74 solar flux units. We simulated the WHI twice using two difference sets of solar wind input: one with the full solar wind and one with the same solar wind conditions but all IMF components are set to zero. There is no magnetic reconnection in the simulation run with no IMF and so there is only the viscous interaction in the solar wind-magnetosphere-ionosphere coupling. It is known that LFM provides larger than realistic transpolar potential (TPP), so we scaled down the TPP of the no IMF run by a factor of $\gamma = 1.54$, that was found by matching the no IMF TPP to the Bruntz et al. [2012a] viscous potential formula. It is important to note that the γ factor was derived from the Bruntz et al. [2012a] potential formula and the no IMF LFM run yet the same γ factor scaled the full IMF LFM run to match the Weimer05 model which is completely unrelated to LFM. We take this mean that the γ factor is accounting for the LFM conductances being too low, and thus the potentials are too high.

We applied the same scaling factor that was found using the no IMF TPP and the Bruntz et al. [2012a] viscous potential formula to the full IMF TPP. When the scaled full IMF TPP was compared to the output of an empirical model, Weimer05, it was shown that the scaled full IMF TPP were in good agreement with Wieimer05 for periods that had southward IMF. For periods that were northward, Weimer05 reached an artificial floor while LFM does not have a minimum TPP value and simply responds to the physical driving. We also compared the no IMF run with the full IMF run, we showed that the periods in which the TPP from the no IMF run was greater than the full IMF run corresponded to periods of northward IMF. This is consistent with recent studies that

have found that northward IMF reduces the viscous interaction and that at small values of northward IMF, the TPP is purely viscous and does not contain any contributions from the reconnection interaction while the southward IMF's TPP is the combination of the viscous and the reconnection interaction.

Since the no IMF run provided reasonably good viscous only potentials, we also simulated the WHI with the B_z set to zero and another run with the B_y set to zero, while all other conditions remain the same. The no-B_z run contains the merging and viscous interaction due to B_y while the no-B_y run contains the merging and viscous interaction due to B_z. It is known that the viscous interaction is unaffected by the B_y and unaffected by negative B_z; therefore the viscous interaction from the no-B_z run is equal to the viscous interaction from the no-IMF run. We found that the full IMF (Φ_{Full}) run can be reconstructed by using a linear combination of three independent runs: the no-B_z (Φ_{0Bz}) run plus the no-B_y (Φ_{0By}) run minus the no-IMF (Φ_{0B}) run such that , $\Phi_{Full} = \Phi_{0Bz} + \Phi_{0By} - \Phi_{0B}$. This is because the full IMF contains one part B_y merging, one part B_z merging, and one part B_z viscous while the addition of the no-B_z with the no-B_y contains two contributions to the viscous interaction, one from each run, which is reduced to one contribution by subtracting out the no-IMF run.

Finally, we artificially modified the amplitude of the solar wind fluctuations present in a high speed stream found in the WHI. We isolated the solar wind fluctuations amplitude in the magnetic field and velocity, then applied a multiplier to the fluctuations to artificially enhance or dampen the fluctuation amplitudes. Using multipliers of $\alpha = 0.5$, 1, and 2, we found that as the fluctuation amplitudes increased from $\alpha = 0.5$ to $\alpha = 2$, the total amount of energy dissipated by the solar wind-magnetosphere-ionosphere system was increased but the efficiency of the energy transfer decreased. This decrease in

energy transfer efficiency was found to be due to the increased presence of northward IMF when the fluctuation amplitudes were increased.

The conclusion is supported by a series of numerical experiments in which the IMF was steady southward B_z except for a short 20-minute period of northward IMF. Each run had the same magnitude of steady southward B_z but the magnitude of the northward IMF was changed between runs. We found that when the IMF transitions from northward to southward, the ionosphere remains in a state of reduced energy transfer for approximately 50 minutes to an hour afterwards where the larger magnitude of northward IMF caused the reduction to be greater. We also verified that the presence of northward IMF was decreasing the total energy by simulating the same runs as before, α = 0.5, 1, and 2, except whenever the IMF was positive, we set the IMF to zero. This will remove all northward IMF from the simulation run while retaining all of the southward IMF. We found that with northward IMF set to zero, the total energy was increased by more than 30% and the efficiency was greater than the original runs.

5.2 Future Work

There are some areas in which future work might prove to be rewarding such as expanding on the lower conductance provided by LFM resulting in potentials that are too high. Since it is suspected that the underestimated electron precipitation in the LFM ionosphere is causing LFM to produce conductances that are too low, it would be useful to dive into the code and forcefully increase the electron precipitation by various factors until a sufficient conductance is obtained. Once the needed factor is known, an investigation of the sources of electron precipitation should pinpoint the reason and physics that are missing from the ionospheric model to account for the needed electron precipitation.

The heliospheric model used in Wiltberger et al. [2012] poorly replicated the solar wind conditions for the WHI and so an investigation of which driver in that heliospheric model can produce solar wind fluctuations would be useful in improving heliospheric models and the understanding underlying physics. It would also be useful to study whether other heliospheric models can reproduce the amplitude of solar wind fluctuations and analyze the differences in physics between the models that can and cannot produce solar wind fluctuations.

References

Akasofu, S.-I. (1981), Energy coupling between the solar wind and the magnetosphere, *Space Sci. Rev., 28*, 121.

Aksnes, A., O. Amm, J. Stadsnes, N. Ostgaard, G. A. Germany, R. R. Vondrak, and I. Sillanpaa (2005), Ionospheric conductances derived from satellite measurements of auroral UV and X-ray emissions, and ground-based electromagnetic data: a comparison, *Ann. Geophys., 23,* 343-358.

Baker, D. N., N. E. Turner, T. I. Pulkkinen (2001), Energy transport and dissipation in the magnetosphere during geomagnetic storms, *J. Atmos. Solar Terr. Phys.,* 63, 421-429, doi:10.1016/S1364-6826(00)00169-3.

Baumjohann, W., and Y. Kamide (1984), Hemispherical Joule heating and the AE indices, *J. Geophys. Res.,* 89, 383.

Belcher, J. W., and L. Davis Jr. (1971), Large-amplitude Alfvén waves in the interplanetary medium, 2*, J. Geophys. Res., 76(16),* 3534–3563, doi:10.1029/JA076i016p03534.

Bhattarai, S. K., R. E. Lopez, R. Bruntz, J. G. Lyon, and M. Wiltberger (2012), Simulation of the polar cap potential during periods with northward interplanetary magnetic field, *J. Geophys. Res.*, *117*, A04219, doi:10.1029/2011JA017143.

Bhattarai, S. K., and R. E. Lopez (2013), Reduction of Viscous Potential for Northward Interplanetary Magnetic Field as seen in the LFM Simulation, *J. Geophys. Res. Space Physics, 118,* doi:10.1002/jgra.50368.

Boyle, C., P. Reiff, and M. Hairston (1997), Empirical polar cap potentials, *J. Geophys. Res.*, *102*(A1), 111 -125, doi:10.1029/96JA01742.

Brekke, A., J. R. Doupnik, and P. M. Banks (1974), Incoherent scatter measurements of E region conductivities and currents in the auroral zone, *J. Geophys. Res., 79,* 3773-3790.

Brekke, A., and C. Hall (1988), Auroral ionospheric quiet summertime conductances, *Ann*. *Geophysicae*, 6, 361—376.

Brekke, A., and J. Moen (1993), Observations of high-latitude ionospheric conductances, *J. Atmos. Terr*. *Phys*., 55, 1493—1512.

Bruntz, R., R. E. Lopez, M. Wiltberger, and J. G. Lyon (2012a), Investigation of the viscous potential using an MHD simulation, *J. Geophys. Res., 117*, A03214, doi:10.1029/2011JA017022.

Bruntz, R., R. E. Lopez, S. K. Bhattarai, K. H. Pham, Y. Deng, Y. Huang, M. Wiltberger, and J. G. Lyon (2012b), Investigating the viscous interaction and its role in generating the ionospheric potential during the Whole Heliosphere Interval, *J. Atmos. Sol. Terr. Phys.*, 10.1016/j.jastp.2012.03.016.

Burke, W. J., M. C. Kelley, R. C. Sagalyn, M. Smiddy, and S. T. Lai (1979), Polar cap electric field structures with a northward interplanetary magnetic field, *Geophys. Res. Lett.*, *6*(1), 21–24, doi:10.1029/GL006i001p00021.

Burke, W. J., D. R. Weimer, and N. C. Maynard (1999), Geoeffective interplanetary scale sizes derived from regression analysis of polar cap potentials, *J. Geophys. Res.*, *104(A5)*, 9989–9994, doi:10.1029/1999JA900031.

Burton, R. K., R. I. Mc Pherron, and C. T. Russell (1975), An empirical relationship between interplanetary conditions and dst, *J. Geophys. Res., 80,* 4204-4214.

Carlowicz, M., and R. E. Lopez (2002), *Storms from the Sun,* Joseph Henry Press, Washington D.C..

Claudepierre, S. G., S. R. Elkington, and M. Wiltberger (2008), Solar wind driving of magnetospheric ULF waves: Pulsations driven by velocity shear at the magnetopause*, J. Geophys. Res., 113*, A05218, doi:10.1029/2007JA012890.

De Lucas, A., W.D. Gonzalez, E. Echer, F.I. Guarnieri, A. Dal Lago, M. R. da Silva, L.E.A. Vieira, and N. J. Schuch (2007), Energy balance during intense and super intense magnetic storms using an Akasofu e parameter corrected by the solar wind dynamic pressure, *J. Atmos. Sol. Terr. Phys., 69,* 1851-1863.

Dungey, J. W. (1961), Interplanetary magnetic field and the auroral zones, *Phys. Rev. Lett.*, Vol. 6, pp. 47-48.

Fedder, J.A., S.P. Slinker, J.G. Lyon, R.D. Elphinstone (1995), Global numerical simulation of the growth phase and the expansion onset for substorm observed by Viking, *J. Geophys. Res.*,*100*(A10), 19083–19093, doi:10.1029/95JA01524.

Fedder, J. A., S. P. Slinker, and J. G. Lyon (1998), A comparison of global numerical simulation results to data for the January 27–28, 1992, Geospace Environment Modeling challenge event, *J. Geophys. Res., 103*, 14,799.

Gosling et al. (1995), The band of solar wind variability at low heliographic latitudes near solar activity minimum: Plasma results from Ulysses rapid latitude scan, *Geophys. Res. Lett, 22,* 3329, doi:10.1029/95GL02163.

Guo, J., X. Feng, B. A. Emery, J. Zhang, C. Xiang, F. Shen, and W. Song (2011), Energy transfer during intense geomagnetic storms driven by interplanetary coronal mass ejections and their sheath regions, *J. Geophys. Res., 116*, A05106, doi:10.1029/2011JA016490.

Hundhausen, A. J. (1995), The solar wind , in Introduction to Space Physics*, edited by M. G. Kivelson and C. T. Russel, pp91-128*, Cambridge University Press.

Iijima, T., and T. A. Potemra (1976), The amplitude distribution of field-aligned currents at northern high latitudes observed by TRIAD, *J. Geophys. Res., 81(13),* 2165–2174, doi:10.1029/JA081i013p02165.

Kamide, Y., and A. D. Richmond (1982), Ionospheric conductivity dependence of electric field and currents estimated from ground magnetic observations, *J. Geophys. Res., 87*, 8331-8337.

Kane, R. P. (2010), Scatter in the plots of Dst(min) versus Bz(min), *Planetary and Space Science, 58*, 1792-1802, doi:10.1016/j.pss.2010.07.026.

Kivelson, M. G., C. T. Russell (editors) (1995), *Introduction to Space Physics*, Cambridge University Press, ISBN 0-521 -45714-9.

Knipp, D. J., et al. (1998), An overview of the early November 1993 geomagnetic storm, *J. Geophys. Res., 103, 26*, 197026,220, doi:10.1029/98JA00762.

Kosch, M. J., T. Hagfors, and K. Schlegel (1998), Extrapolating EISCAT Pedersen conductancces to other parts of the sky using ground-based TV auroral images, *Ann. Geophys., 16,* 583-588.

Koskinen, H.E.J., and E. I. Tanskanen (2002), Magnetospheric energy budget and the epsilon parameter, *J. Geophys. Res., 107(A11),* 1415, doi:10.1029/2002JA009283.

Liemohn, M. W., Jazowski, M., Kozyra, J. U., Ganushkina, N., Thomsen, M. F., J. E. Borovsky (2010) CIR versus CME drivers of the ring current during intense magnetic storms, *Proc. R. Soc. A 466*, 3305–3328, doi:10.1098/rspa.2010.0075.

Lilensten, J., P. L. Blelly, W. Kofman, and D. Alcayde (1996), Auroral ionospheric conductivities: a comparison between experiment and modeling, and theoretical f10.7-dependent model for EISCAT and ESR, *Ann. Geophys., 14*, 1297-1304.

Lopez, R. E., and J. W. Freeman (1986), Solar wind proton temperature-velocity relationship, *J. Geophys. Res., 91(A2),* 1701–1705, doi:10.1029/JA091iA02p01701.

Lopez, R. E., M. Wiltberger, J. G. Lyon, C. C. Goodrich, and K. Papadopoulos (1999), MHD simulations of the response of high-latitude potential patterns and polar cap boundaries to sudden southward turnings
of the interplanetary magnetic field, *Geophys. Res. Lett.*, *26(7)*, 967–970, doi:10.1029/1999GL900113.

Lopez, R. E., R. Bruntz, E. J. Mitchell, M. Wiltberger, J. G. Lyon, and V. G. Merkin (2010), Role of magnetosheath force balance in regulating the dayside reconnection potential, *J. Geophys. Res.*, *115*, A12216, doi:10.1029/2009JA014597.

Lopez, R. E., Bhattarai, S. K., Bruntz, R., Pham, K., Wiltberger, M., Lyon, J. G., Deng, Y., Huang, Y., (2012). The Role of Dayside Merging in Generating the Ionospheric Potential During the Whole Heliosphere Interval, *J. Atmos. Solar Terr. Phys*., doi:10.1016/j.jastp.2012.03.001.

Lopez, R. E., R. Bruntz, and K. Pham (2014), Linear separation of orthogonal merging component and viscous interactions in solar wind-geospace coupling, *J. Geophys. Res. Space Physics, 119,* 7566–7576, doi:10.1002/2014JA020153.

Lu, G., et al. (1998), Global energy deposition during the January 1997 magnetic cloud event, *J. Geophys. Res., 103(A6),* 11685–11694, doi:10.1029/98JA00897.

Lyon, J. G., J. A. Fedder, and C. M. Mobarry (2004), The Lyon-Fedder-Mobarry (LFM) global MHD magnetospheric simulation code, *J. Atmos. Sol. Terr. Phys.*, *66*, 1333– 1350, doi:10.1016/j.jastp.2004.03.020.

McIntosh, S. W., B. D. Pontieu, M. Carlsson, V. Hansteen, P. Boerner, M. Goossens (2011), Alfvénic waves with sufficient energy to power the quiet solar corona and fast solar wind, *Nature*, 475 (7357): 477 doi:10.1038/nature10235.

Merkin, K., V., Papadopoulos, G. Milikh, A. S. Sharma, X. Shao, J. Lyon, and C. Goodrich (2003), Effects of the solar wind electric field and ionospheric conductance on the cross polar cap potential: Results of global MHD modeling, *Geophys. Tes. Lett.*, *30(23)*, 2180, doi: 10.1029/2003GL017903.

Mitchell, E. J., R. E. Lopez, R. J. Bruntz, M. Wiltberger, J. G. Lyon, R. C. Allen, S. J. Cockrell, and P. L. Whittlesey (2010), Saturation of transpolar potential for large Y component interplanetary magnetic field, *J. Geophys. Res., 115,* A06201, doi:10.1029/2009JA015119.

Monreal-MacMahon, R. and W.D. Gonzalez (1997), Energetics during the main phase of geomagnetic superstorms, *J. Geophys. Res.,* 102 (A7), 14199-14207.

Newell, P. T., T. Sotirelis, K. Liou, and F. J. Rich (2008), Pairs of solar wind-magnetosphere coupling functions: Combining a merging term with a viscous term works best, *J. Geophys. Res.*, *113*, A04218, doi:10.1029/2007JA012825.

O'Brien, P., and R. I. McPherron (2000), An empirical phase space analysis of ring current dynamics: solar wind control of injection and decay, *J. Geophys. Res., 105,* 7707-7719.

Perreault, P., and S.-I. Akasofu (1978), A study of geomagnetic storm, *Geophys J. of the Royal Astro. Soc., 54,* 547-573.

Pham, K. H., R. J. Bruntz, and R. E. Lopez (2014), The role of the amplitude of solar wind fluctuations on solar wind-magnetosphere coupling, in review.

Philips, J., et al. (1995a), Ulysses solar wind plasma observations from pole to pole, *Geophys. Res. Lett., 22,* 3301, doi:10.1029/95GL03094.

Raeder, J., J. Berchem, and M. Ashour-Abdalla (1998), The Geospace Environment Modeling Grand Challenge: Results from a Global Geospace Circulation Model, *J. Geophys. Res.,* 103, 14,787.

Reiff, P. H. (1984), Models of auroral-zone conductances, in *Magnetospheric Currents,* Geophys. Monogr. Ser., vol 28, edited by T. A. Potemra, p. 180, Washington, D. C..

Richardson, I. G., et al. (2006), Major geomagnetic storms (Dst ≤ −100 nT) generated by corotating interaction regions*, J. Geophys. Res., 111,* A07S09, doi:10.1029/2005JA011476.

Richmond, A. D., and Y. Kamide (1988), Mapping Electrodynamic Features of the High-Latitude Ionosphere from Localized Observations: Technique, *J. Geophys. Res.*, *93*(A6), 5741–5759, doi:10.1029/JA093iA06p05741.

Ridley, A. J., K. C. Hansen, G. To´th, D. L. De Zeeuw, T. I. Gombosi, and K. G. Powell (2002), University of Michigan MHD results of the Geospace Global Circulation Model metrics challenge, *J. Geophys. Res.,* 107(A10), 1290, doi:10.1029/2001JA000253.

Ridley, A. J., and E. A. Kihn (2004), Polar cap index comparisons with AMIE cross polar cap potential, electric field, and polar cap area, *Geophys. Res. Lett.*, *31*, L07801, doi:10.1029/2003GL019113.

Sibeck, D. G., R. E. Lopez, and E. C. Roelof (1991), Solar Wind Control of the Magnetopause Shape, Location, and Motion, *J. Geophys. Res.*, *96*(A4), 5489–5495, doi:10.1029/90JA02464.

Space Studies Board (2008), *Severe Space Weather Events- Understanding Societal and Economic Impacts*, A Workshop Report, The National Academies Press, Washington, D. C..

Tsurutani, B. T., et al. (2006, Corotating solar wind streams and recurrent geomagnetic activity: A review, *J. Geophys. Res., 111*, A07S01, doi:10.1029/2005JA011273.

Vickrey, J. F., R. R. Vondrak, and S. J. Matthews (1981), The diurnal and latitudinal variation of auroral zone ionospheric conductivity, *J. Geophys. Res., 86,* 65-75.

Wang, W., Wiltberger, M., Burns, A. G., Solomon, S., Killeen, T. I. (2004), Initial results from the center for integrated space weather modeling coupled magnetosphere ionosphere thermosphere model: Ionospheric and thermospheric responses. *J. Atmos. Solar Terr. Phys.*, *66*, 1425-1441, doi:10.1016/j.jastp.2004.04.008.

Webb, D. F., and R. A. Howard (1994), The solar cycle variation of coronal mass ejections and the solar wind mass flux, *J. Geophys. Res., 99*(A3), 4201–4220, doi:10.1029/93JA02742.

Weimer, D. R. (2005), Improved ionospheric electrodynamic models and application to calculating Joule heating rates, *J. Geophys. Res.*, *110*, A05306, doi:10.1029/2004JA010884.

Wiltberger, M., Wang, W., Burns, A., Solomon, S., Lyon, J. G., Goodrich, C. C. (2004), Initial results from the coupled magnetosphere ionosphere thermosphere model: Magnetospheric and ionospheric responses. *J. Atmos. Solar Terr. Phys. 66*, 1411 -1423, doi:10.1016/j.jastp.2004.03.026.

Wiltberger, M., L. Qain, C. -L. Huang, W. Wang, R. E. Lopez, A. G. Burns, S. C. Solomon, Y. Deng, Y. Huang (2012), CMIT study of CR2060 and 2068 comparing L1 and MAS solar wind drivers, *J. Sol. Terr. Phys.*, doi:10.1016/j.jastp.2012.01.005.

Zirker, J. B. (1977), Coronal holes and high-speed wind streams, *Rev. Geophys., 15(3),* 257–269, doi:10.1029/RG015i003p00257.

Zwickl, R. D., L. F. Bargatze, D. N. Baker, C. R. Clauer, and R. L. McPherron (1987), An evaluation of the total magnetospheric energy output parameter, Ut, in Magnetotail Physics, edited by A. T. Y. Lui, Johns Hopkins University Press, 155-159.

Biographical Information

Kevin H. Pham received his Bachelor's of Science degree in Physics and also in Mathematics from the University of Washington at Seattle, in 2009. He immediately entered graduate school pursuing a B.S. to Ph.D. in Physics at the University of Texas at Arlington. He joined the Lopez Research Group and began research under Dr. Ramon E. Lopez in May of 2010. As a part of the group, his responsibilities included overseeing a variety of undergraduate projects, and managing the weekly group meetings. He also planned and built a number of computer systems and clusters for the lab. He is interested in the magnetospheric and ionospheric dynamics under quickly varying solar wind conditions. This interested is extended towards application to other planetary bodies and space travel. He would like to do more work improving the accuracy of MHD simulations. His immediate post-graduation plans are to find a Post-doctoral position, preferably at NASA, and to eventually transition to a full-time research.